UNIVERSITAT POLITÈCNICA DE CATALUNYA
BARCELONATECH
Escola d'Enginyeria de Telecomunicació
i Aeroespacial de Castelldefels

Institut d'Estudis
Espacials de Catalunya

TREBALL DE FI DE GRAU

TFG TITLE: Low-frequency effects in the LISA temperature diagnostics subsystem

DEGREE: Double bachelor's degree in Aerospace Systems Engineering and Telecommunications Systems Engineering

AUTHOR: Alba Gonzálvez Rubio

ADVISOR: Juan Jose Ramos Castro, PhD.

SUPERVISOR: Miquel Nofrarias Serra, PhD.

DATE: October 17, 2022

Títol: Low-frequency effects in the LISA temperature diagnostics subsystem
Autor: Alba Gonzálvez Rubio

Director: Juan Jose Ramos Castro, PhD.

Supervisor: Miquel Nofrarias Serra, PhD.

Data: 17 d’octubre de 2022

Resum

L’objectiu principal de la tesi és determinar la contribució del nivell de soroll per a un prototip electrònic Laser Interferometer Space Antenna (LISA). La tesi cobreix coneixements sobre freqüències submilihertz, des del rendiment teòric i experimental del soroll del sensor fins a mesures de temperatura. El projecte pretén contribuir a la recerca de la Institut d’Estudis Espacials de Catalunya (IEEC) que es va centrar en el desenvolupament d’equips d’alta estabilitat per al primer observatori espacial d’ones gravitacionals de European Space Agency (ESA) anomenat LISA. Aquesta missió pionera millorarà el coneixement sobre nombrosos conceptes intrigants sobre l’inici i l’evolució de l’univers. Per exemple, els forats negres i la formació de galàxies juntament amb la teoria de la relativitat general. No obstant això, les fluctuacions de temperatura provinents de l’electrònica de la nau espacial podrien pertorbar les mesures de ones gravitacionals, per tant, aquí és on la tesi fa incís. En primer lloc, es fa una breu introducció sobre les ones gravitacionals i la necessitat de la seva detecció. A més d’això, la tesi presenta els requisits i anàlisis de temperatura de LISA. Posteriorment, la tesi analitza, teòricament i experimentalment, el coeficient de temperatura d’un prototip d’electrònica LISA, amb el posterior estudi de l’anàlisi de la projecció de soroll. La tesi s’ha basat en l’esforç considerable realitzat prèviament per l’equip IEEC.

Title : Low-frequency effects in the LISA temperature diagnostics subsystem
Author: Alba Gonzálvez Rubio

Advisor: Juan Jose Ramos Castro, PhD.

Supervisor: Miquel Nofrarias Serra, PhD.

Date: October 17, 2022

Overview

The dissertation main purpose is to determine the noise level contribution for a LISA electronic prototype. The thesis covers insights over sub-millihertz frequencies, from theoretical and experimental sensor noise performance to temperature measurements. The project aims to contribute to the IEEC research focused on developing high stable equipment for the ESA's first space based gravitational wave observatory called LISA. This pioneering mission will enhance the knowledge about numerous intriguing concepts regarding the beginning and evolution of the universe. For instance, black holes and galaxy formation along with general relativity theory. Notwithstanding, the temperature fluctuations coming from the spacecraft electronics could perturb the Gravitational Wave (GW) measurements, hence this is where the dissertation takes over. Firstly, a brief introduction regarding the GW and the need for their detection is provided. Further to this, the dissertation presents the LISA temperature requirements and analyses. Afterwards, the dissertation analyses, theoretically and experimentally, the temperature coefficient for a LISA electronics prototype, with the subsequent study of the noise projection analysis. The thesis has been built on the considerable effort previously made by the IEEC team.

“If you want something you’ve never had,
you’ve got to do something you’ve never done before.”
– Thomas Jefferson

CONTENTS

LIST OF FIGURES

LIST OF TABLES

ACRONYM LIST

ADC Analog-to-Digital Converter. 14, 18, 22–24, 26–31, 37, 70

AFB Analog Front-end Board. 18

ASD Amplitude Spectrum Density. xi, xii, 38, 39, 42, 43, 46–50, 52, 55, 56, 67, 68

ATCU Air Thermal Control Unit. 16, 63, 77, 78

CMB Cosmic Microwave Background. 6

CPSD Cross Power Spectral Density. 44

DAC Digital-to-Analog Converter. 18, 22

DC Direct Current. 22

DMM Digital Multimeter. xi, xii, 34, 35, 43, 46–49, 51, 54–56

DPB Digital Processing Board. 18

DRS Disturbance Reduction System. 12

EBB Elegant Breadboard. xi, xii, 18, 23, 24, 27, 34–37, 40–43, 46–52, 54–57, 62, 63, 66–70

EH Electrode Housing. xi, 13

ESA European Space Agency. iv, vi, 5, 12, 15, 18, 70

FDA Fully Differential Amplifier. 22, 25, 26, 28, 29

FEE Front-End Electronics. 18, 37, 50

FSV Full Scale Voltage. 26

FT Fourier Transform. 45, 46

GRS Gravitational Reference Sensors. xi, 13

GW Gravitational Wave. vi, 5–8, 10, 12, 18

GWs Gravitational Waves. 5–10, 12, 15

IA Instrumentation Amplifier. 23, 24

ICE-CSIC Institute of Space Science. 70

IEEC Institut d'Estudis Espacials de Catalunya. iv, vi, 5, 62, 63, 70

LETS LISA Enhancement Temperature Subsystem. 5, 15, 18, 22, 63, 64, 67, 69, 70

LIGO Laser Interferometer Gravitational-Wave Observatory. 9

LISA Laser Interferometer Space Antenna. iv, vi, xi, 5, 7, 10–16, 18, 51, 52, 62, 65, 69, 70

LPF LISA Pathfinder. xi, 12–15, 18, 19, 24

LTP LISA Technology Package. 12, 14, 15

MCU Microcontroller Unit. 18, 22, 37

MUX Multiplexor. 24

NASA National Aeronautics and Space Administration. 5

NTC Negative Temperature Coefficient. xi, 19–22, 34, 35, 67

OA Operational Amplifier. 22, 29

P Peltier. 65

PCB Printed Circuit Board. 18

PDB Power Distributing Board. 18

PSD Power Spectrum Density. 44–46

PTA Pulse Time Array. 6

RMS Root Mean Square. 23, 27

RTD Resistance Temperature Detector. 19, 20

SDS Scientific Diagnostic Subsystem. 5

SMART Small Missions for Advanced Research in Technology. 12

TB Test Bench. xii, 63, 65, 67, 68, 70

TF Transfer Function. 34, 44, 46, 57–63

TM Test Mass. xi, 5, 12–14

TMS Temperature Measurement Subsystem. 5, 18, 19, 67, 69, 70

TMs Test Masses. 12

WB Wheatstone Bridge. 21, 22, 28, 29, 37, 50, 51, 57–59, 61, 62, 67, 70

ACKNOWLEDGEMENTS

Undertaking this dissertation has been a challenging experience for me, and I am overwhelmed to concede my depth to the great deal of support and assistance that I have received. I would first like to give my warmest thanks to my thesis advisor Dr. Juan Jose Ramos Castro and supervisor Dr. Miquel Nofrarias Serra for the golden opportunity they gave me to widen my research from several perspectives in a field I am precisely interested in. Notwithstanding their busy schedules, they managed to advice and steer me in the right direction whenever I ran into obstacles during the dissertation. They outshine in their particular fields and they undeniably transmit an inspiring motivation I gladly felt. Their passionate participation and input contributed enormously to the successful completion of the project.

I would like to earnestly acknowledge the sincere efforts and precious time given by Dr. David Roma Dollase and Victor Martín Hernández, and I am gratefully indebted to their very valuable guidance and opinions throughout all the experimental procedures which were satisfyingly performed with an experienced insight.

Finally, I must express my very profound gratitude to my parents for providing me with constant support and unceasing encouragement through my day-to-day life and the course of researching and writing this thesis. I am also very thankful for the great fellowship provided by my colleague and friend Biel Bonastre who made the experience more pleasant. This accomplishment would not have been feasible without them. Thank you.

CHAPTER 1. INTRODUCTION

This dissertation presents the measurement of temperature at the micro-Kelvin level in the frequency range of the milli-Hertz. Such precise measurements are required as an essential part of ESA-National Aeronautics and Space Administration (NASA) space mission that aims to design, built and operate a space-borne gravitational wave detector. LISA is a space-based gravitational wave observatory that pursues to perform the detection and observation of gravitational waves and it presumes to revolutionize many fields of study, namely, astrophysics and cosmology among others. This large-class mission is addressed to the science theme of Gravitational Universe, and is expected to be launch in 2034.

The IEEC boost the spanish contribution to the design of Scientific Diagnostic Subsystem (SDS) as the core element of LISA Payload. Three different fields can be distinguished in SDS. One studies the high energy radiation environment responsible for TMs charging and analyse the charge generation in TMs, a second develops an improved more compact magnetic diagnostic system and the last is focused on the Temperature Measurement Subsystem (TMS) under LISA Enhancement Temperature Subsystem (LETS) ESA contract.

The work presented in this dissertation is devoted to the latter aforementioned field which its main objective is the design of a prototype temperature subsystem for LISA (TRL4 [11]) in order to increasing one order of magnitude performance $1\ \mu K/\sqrt{Hz}$ down to $1\ mHz$. A first introduction of the Gravitational Waves (GWs) and its detection is provided. Afterwards, there is an overview of the LISA mission and a foreword of the temperature requirements of the TMS is presented.

1.1. Gravitational waves

The existence of GW is connected to the General Theory of Relativity introduced by Albert Einstein in 1916 [12]. This theory introduces the GW as propagation of the gravitational fields. According to Einstein's believes, GWs are born in a source of gravitational field whose structure varies with time.

Einstein's calculations postulates that whirling masses, to cite an instance, neutron stars or two black holes spiraling together radiate ripples outwards at the speed of light in space-time. These gravitational perturbations distort the space-time geometry.

The characteristic pattern of the wave's distortion of the space-time as it travels is basically described by the two polarization states that GW present. This particular feature involves free falling bodies expanding in one direction while having their perturbations going perpendicular to the wave's propagation. The distance between these free falling masses changes in the perpendicular direction of the passing GW in both polarization modes and this property is the key aspect to measure them. Assuming that a GW propagating in the z-direction of the Cartesian coordinates is conceived, the space stretches at the maximum amplitude in the plane x-y after a time t is passed. Consequently, one half-period later ($t + T/2$), space shortens by its maximum amplitude, thus at time $t + T$, when a full period is perceived, it expands to its maximum. Further to this point, space is deformed in quite the reverse phase of x-direction when y-direction is conceived.

According to the gravitational relativity, the key properties of the GWs are: (i) moving through empty space at the speed of light, (ii) present two polarization modes (the plus-polarization '+' and cross-polarization 'x') and (iii) are transverse to the direction of propagation.

Figure 1.1 draws a suitable picture of both polarization modes.

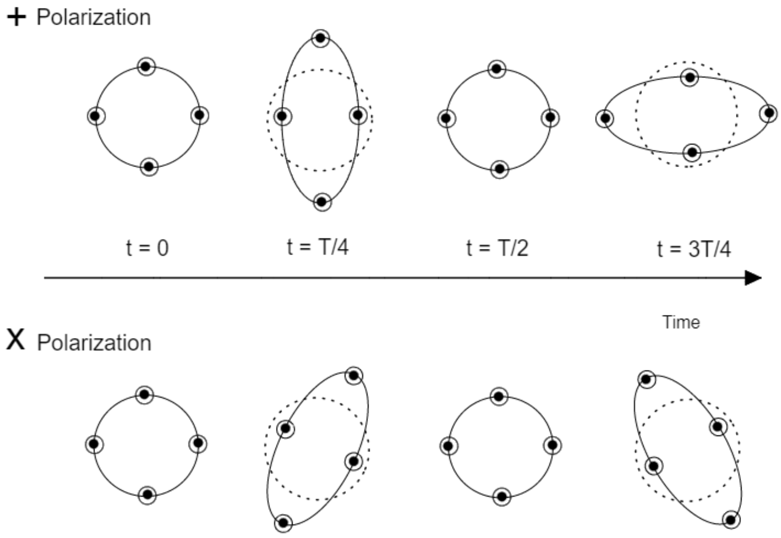

Figure 1.1: Freely falling macroscopic bodies (represented as black dots). The gravitational wave direction is perpendicular to the ring. Both polarization modes are shown ('+'(top) and 'x'(bottom))

When GWs are discussed, the most common describing parameter is the strain amplitude *h*. *h* is twice the relative change displacement between two masses due to a GW. As aforementioned, this change in displacement occurs in the plane transverse towards the radiation's direction, and consequently, there is a stretch along one axis and a squeeze along the orthogonal axis.

$$h=\frac{2\triangle d}{d} \tag{1.1}$$

Whether a parallelism with the electromagnetic spectrum is conceived, notice that the GW spectrum also covers a wide frequency range. This frequency sweep can be divided into four different bands as detailed in [13]. (i) *Ultra low frequency band* 10^{-18} to 10^{-13} Hz (ii) *Very low frequency band* 10^{-9} to 10^{-7} Hz (iii) *Low frequency band* 10^{-5} to 1 Hz (iv) *High frequency band* 1 Hz to 10^{4} Hz.

(i) *Ultra low frequency band* (10^{-18} to 10^{-13} Hz): Observing the polarization of the Cosmic Microwave Background (CMB).

(ii) *Very low frequency band* (10^{-9} to 10^{-7} Hz) : The propagation of GWs across the line of sight of pulsar can affect pulse arrival times. A known use to detect and analyse GWs is an array of millisecond pulsars. A Pulse Time Array (PTA) is a set of pulsars which is analysed to search for correlated signatures in the pulse arrival times. A GW detection would result from a detailed investigation of the correlation between arrival times of pulses emitted by the millisecond pulsars as a function of the pulsars' angular separations.

(iii) *Low frequency band* (10^{-5} to 10^{-1} Hz): LISA will perform GW's detection at 10^{-4} to 1 Hz. To constrain the level of low frequency GWs, a method known as doppler tracking of spacecraft is proposed. Doppler tracking antennas measure the relative distance-change. The development of further GW detection procedures has lead to challenging methods for instance ASTROD I.

In our Galaxy, some relevant sources for these high level missions are galactic binaries (neutron stars, white dwarfs) and supermassive black hole binaries among others.

(iv) *High frequency band* (1 Hz to 10^4 Hz): Detection efforts in the high frequency regime are precisely dominated by Earth-based GW detectors. Laser interferometers and resonant mass antennas exceed in this band. Notwithstanding, at frequencies further down than 1 Hz, the aforementioned detectors present insurmountable noise challenges due to Newtonian gravity gradient. Thus, to expose waves beneath this edge, space detectors are required. It is to be noted that neutron stars and stellar-mass black holes are gravitational wave sources that outline in this band.

Adding a low-frequency GW observatory will be a new open gate regarding the universe observation. In fact, observing GWs from cosmic sources would allow an exquisite exploration of the inaccessible universe where gravity is manifested in countless ways.

The on-ground detectors cover the detection of GWs in *High frequency band* whereas the *Low frequency band* will be covered by the space-based GW detector LISA. Figure 1.2 shows the GW spectrum.

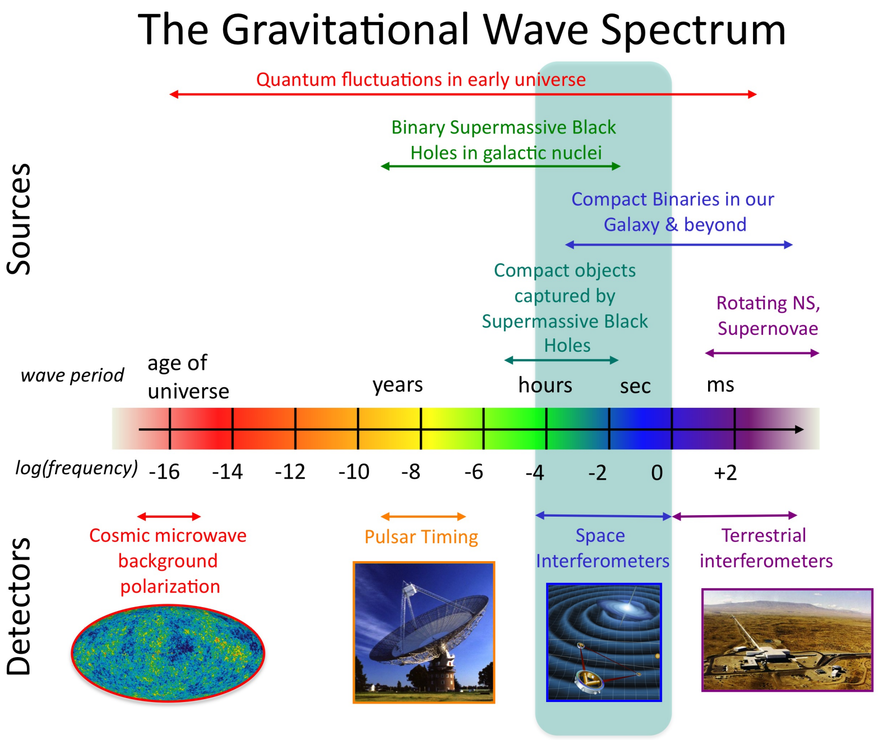

Figure 1.2: Gravitational-wave spectrum, together with potential sources and relevant detectors [1].

1.1.1. Ground-based GW detectors

Two types of detectors have been used to detect GWs. In the current section, a proper description of the resonant mass detectors and the interferometric detectors [14] is provided. They both perform in the *High frequency band*.

1.1.1.1. Resonant mass detectors

Notwithstanding the title of this chapter, it is important to emphasize here the pioneering work of Joseph Weber that fomented an investigation of the gravitational waves detection. Weber suggested that GW could indeed be measured and started the field of resonant mass detectors. Such detectors are massive cylindrical solids whose eigen modes could be excited when GWs pass by. A detailed explanation of eigen modes is provided in [15].

As Einstein introduced a mass quadruple harmonic oscillator could be excited by gravitational radiation. Weber's effort lead to Einstein theory experimental demonstration. Weber's first GW detector was a resonant bar. Resonant mass detectors are cylindrical bars that are expected to vibrate at their resonance frequencies when a GW passes by. Figure 1.3 illustrates the scheme of a resonant mass detector.

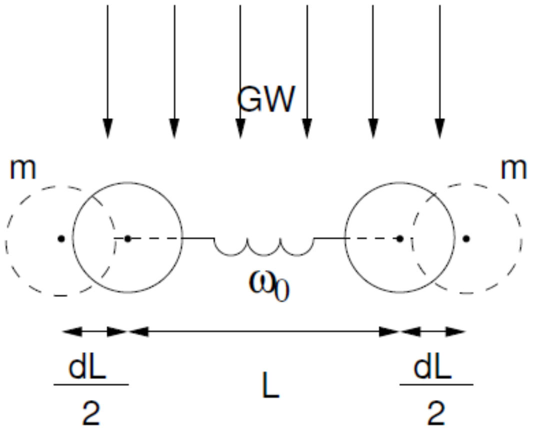

Figure 1.3: Resonant mass detector scheme [2].

The continued progression in this field, allowed achieving sensitives three orders of magnitude above the first ones. Figure 1.4 presents the sensitivities for several resonant mass detectors.

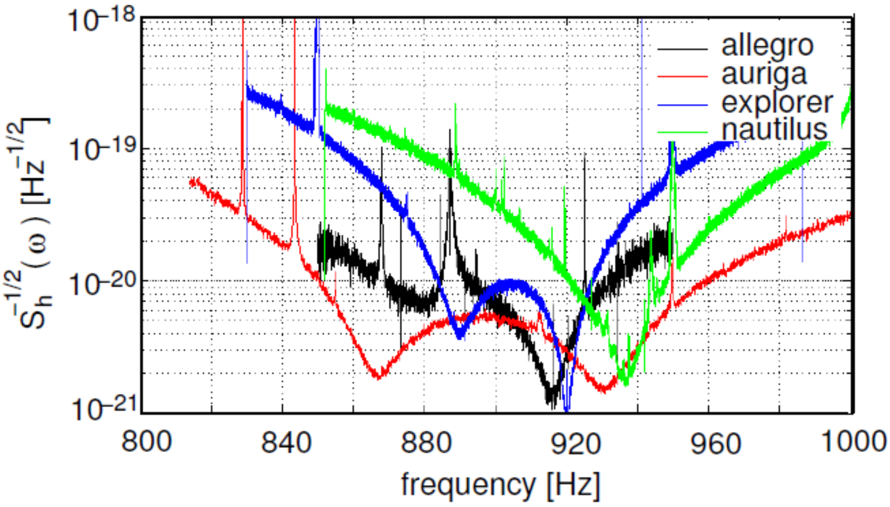

Figure 1.4: Strain sensitivities of different resonant mass detectors [3].

1.1.1.2. Interferometric detectors

Using interferometers as GWs detectors was an alternative method proposed in the 1970s. Interferometric detectors use laser interferometry to measure the distance fluctuation between two isolated bodies. Advanced Laser Interferometer Gravitational-Wave Observatory (LIGO) and Virgo are well-known detectors that have successfully detected GWs.

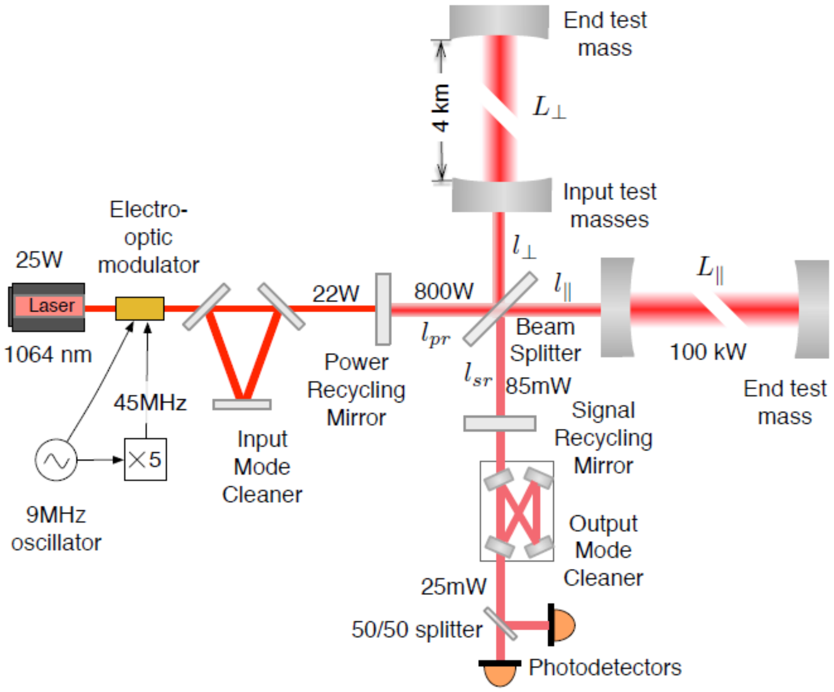

Figure 1.5: Layout of an Advanced LIGO detector [4].

Figure 1.5 represents a schematic of a generic laser interferometer detector. Notice that to identify GWs two arm-links are required. The laser is diverged in two beams that are inserted in two optical arms. When a proper oriented GW passes, the relative length of the arms slightly changes, one arm is squeezed whilst the other is stretched. By means of recombining the beams coming from both arms it is possible to evaluated their respective phase shift. The phase variation can be computed by Eq. 1.2 [16].

$$\delta_\phi = 2h_+ \frac{\omega_L}{\Omega_{GW}} \sin \frac{\Omega_{GW}\tau}{2} \tag{1.2}$$

where ω_L is the angular laser frequency and Ω_{GW} the angular frequency of the GW induced with a polarized strain amplitude h_+ aligned with the arms. τ ($\tau = \frac{2L}{c}$) represents the time that the beam needs to complete twice the distance between the separated masses of a single arm L.

By means of using Fabry-Pérot [17] cavities as resonators, the effective length L is amplified by a factor of $\approx\ 100$.

These detectors are sensitive to several noise sources for instance, seismic noise, thermal noise, photon electron shot noise and gravity gradient noise among others. Prominence must be given to the fact that at high frequency regime the shot noise predominates whereas in the low, seismic and gradient noise dominates the measurements. Since seismic noise makes it difficult for ground-based detectors to work below $1\ Hz$, an interferometric GW space-detector called Laser Interferometry Space Antenna (LISA) is proposed.

Be that as it may, it is paramount to highlight that ground-based interferometers are currently active and under construction. A third generation is in planning phase. Reportedly, the European detector called Einstein Telescope will be the focal point of this next generation. The arms of the equilateral triangle with each corner being the vertex for two detectors (one for low frequency $1-250\,Hz$ and the other for high frequency $10-10\,kHz$, GWs) will be $10\ Km$ long. To reduce seismic and gravity noise its facility will be located underground, and to minimize the thermal noise, it will be cryogenically cooled.

1.2. LISA mission

LISA mission will complement the current knowledge about the beginning, evolution and structure of the universe. Its main objective is to detect gravitational waves from distant systems, namely, supermassive black holes, extreme mass ratio spirals, among other exotic possibilities. These sort of sources correspond to heavier objects in wider orbits than in LIGO's research. It is alleged that studying GWs provides us with a powerful new probes regarding General Relativity and black hole theory.

LISA design is a proposal for a space-borne gravitational wave detector in the bandwidth between $0.1\ mHz$ to $1\ Hz$. Interferometric ground-based detectors are not used in this operating band due to the local gravitational noise. Several events for instance, seismic noise sources, meteorological phenoms and moving objects can prevent GWs detection from happening. Be that as it may, space-based detectors are not affected by these noise sources and they can present rather long arm-length and perform GWs detection in the low frequency range.

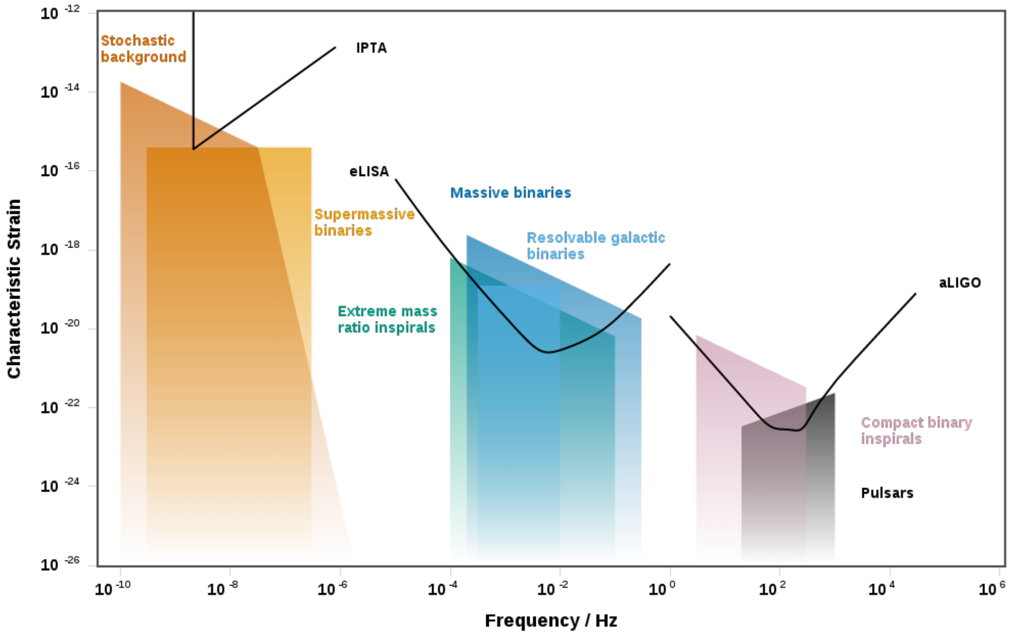

Figure 1.6: Strain sensitivities of LISA [5].

The detector itself consists of three identical spacecraft that form an equilateral triangle separated by $2.5 \cdot 10^6\ Km$, as shown in Figure 1.7. LISA laser links between each pair of satellites works as a Michelson interferometer [18] with a third to get information of the system redundancy and the wave polarization.

The constellation orbits around the Sun with 20° of delay with respect to the Earth. The plane of the triangle has an inclination of 60° with respect to the ecliptic plane in order to achieve the utmost stable infrastructure. Further to this, during a whole orbit around the Sun, the satellite constellation also completes a whole rotation around its center.

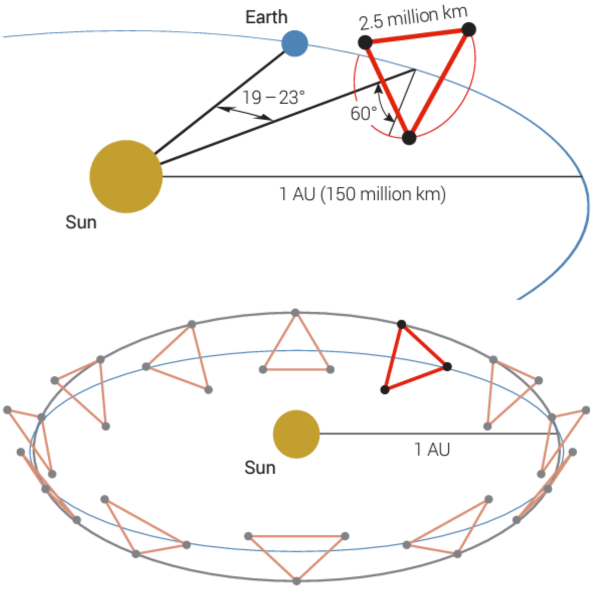

Figure 1.7: Depiction of LISA orbit [6].

Each satellite contains two vacuum enclosures housing a $46\ mm$ cube of gold-platinium alloy known as TM in nominal free fall. These $1.96\ Kg$ solids act as end mirrors of the interferometer. The optical path's length between the TM will change when a GW comes across.

LISA will detect GWs by measuring the differential optical path length modulation along the three sides of a triangular configuration. Thereby, the instrument should operate continuously and light with a wavelength of $\lambda = 1064\ nm$ should be received and transmitted in both arms' directions to gather proper measurements.

When considering the selection of materials, two environmental disturbances have to be noted, the power dissipation perturbations regarding onboard avionics and those related to the output power of the Sun.

LISA proposes several thermal shields to isolate the optical bench from the thermal disturbances originated by solar radiation and electronics. To minimize such undesired changes the following materials are considered: ULE, Clearceram and Zerodur. Such a low thermal expansion coefficient is essential to reach this level of thermal stability.

1.2.1. LISA Pathfinder mission

LPF was one of ESA's Small Missions for Advanced Research in Technology (SMART) that was essentially recognized to test the fundamental elements involved in LISA-based gravitational wave observatory. Having to couple with flight hardware that cannot be tested on the ground due to Earth-induced noise led to LPF mission. The mission carried two payloads, the LISA Technology Package (LTP) and the Disturbance Reduction System (DRS).

The LPF leader requirement was devoted to measure the residual differential acceleration spectral density between Test Masses (TMs) in the band $1-30\ mHz$, as shown in Figure 1.8 .

$$S_{\triangle a}^{1/2}(\omega) \leq 3 \cdot 10^{-14} \cdot \left[1 + \left(\frac{\omega/2\pi}{3mHz} \right)^2 \right] ms^{-2} Hz^{-1/2} \tag{1.3}$$

In order to validate the in-space performance of the different technologies to be used in LISA , the LPF scheme as shown in Figure 1.9 was suggested. The idea of shrinking one LISA arm from $5 \cdot 10^6\ Km$ to $30\ cm$ and allocated it in a single spacecraft was introduced. The short arm-length prevents LPF from detecting GWs, but converts it into a test bench which allows the measurement procedure.

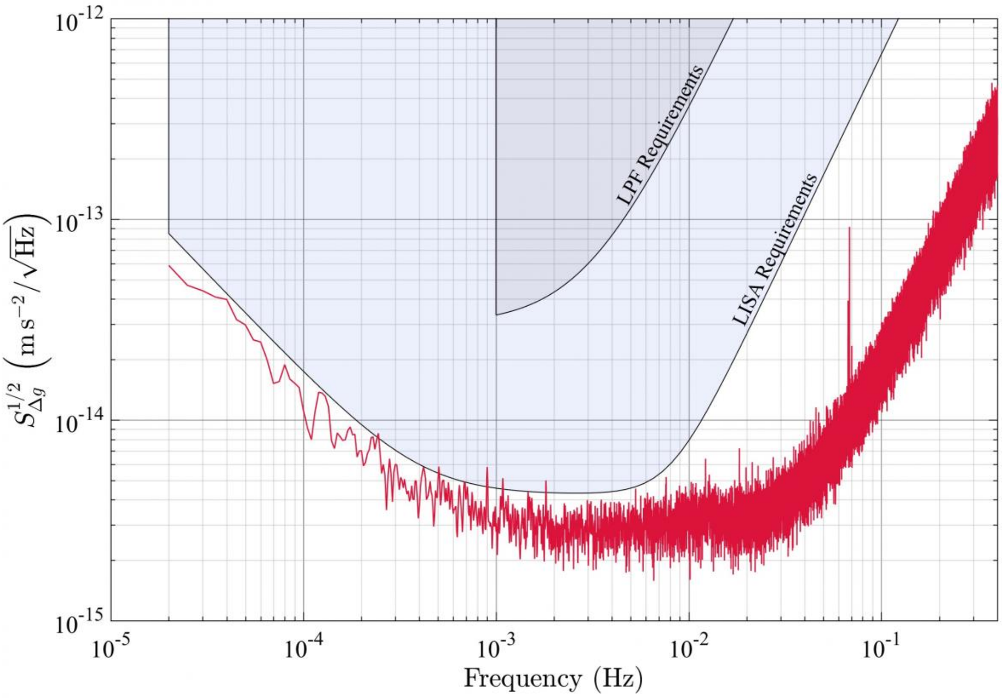

Figure 1.8: Acceleration noise requirement for LPF and LISA [7].

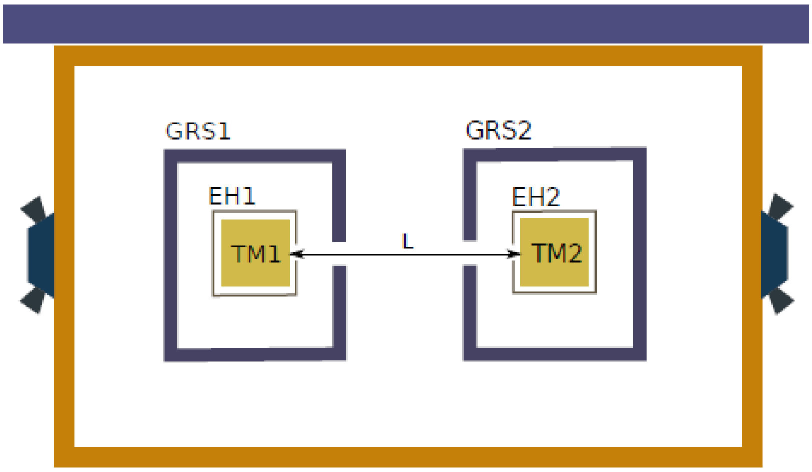

Figure 1.9: Simplification of LTP scheme: two GRS. Each TM is located inside an EH. Each EH hosts a series of electrodes that provide electrostatic sensing and control of the position and attitude of the TM with respect to the satellite. At the same time, series of precision thrusters control the attitude of the spacecraft [7].

The essence of construction for LISA was focused on keeping any differential residual acceleration noise of the TMs below the requirements. Such high level of performance was not possible on the ground as setting TMs in an accurate free fall for long intervals of time was infeasible.

The residual acceleration noise was quantified once the satellite was in orbit and the contributions to total power spectral density can be estimated by a noise model. Among these noise sources, several are identified and eliminated when specific parameters are adjusted, notwithstanding those related to measurable fluctuations of physical parameters involve an accurate system characterization with its particular transfer functions to suppress noise disturbances. Besides these former cases, it was also important to consider noise perturbations that lies at the root of solar radiation or cosmic rays and cannot be erased by any of the prior methods as it was previously mentioned.

1.3. Thermal diagnostics subsystem

One of the utmost important lesson learnt from LPF in terms of performance regarding the diagnostic subsystem achieving the required $10\,\mu K/\sqrt{Hz}$ in the mission band of $1\,mHz$ $<$ f $<$ $30\,mHz$, is the slight deviation present in the low frequency bin due to the coupling of temperature drift on-board with non-linearities in the Analog-to-Digital Converter (ADC). Knowing that this effect also affects the milliHertz band, it allows a considerable improvement in the read-out noise contribution for the LISA temperature diagnostics subsystem.

This section focuses on the aspects related to the thermal effects in the LTP that set the requirements of the thermal diagnostic subsystem.

1.3.1. Thermal disturbances

The total noise permitted for the residual acceleration is defined by Eq. 1.3. Instrumental and environmental perturbing phenomenons could hugely contribute in such important consideration.

Random temperature fluctuations insert noise in the system using various mechanisms. A proper characterization of these causes will lead to determine suitable temperature limitations that fit in LTP requirements. Total thermal contributions should not exceed $10\ \%$ of the total acceleration noise. Hence, it is required that

$$S_{\triangle a}^{1/2}(\omega) \leq 3 \cdot 10^{-15} \cdot \left[1 + \left(\frac{\omega/2\pi}{3mHz}\right)^2\right] ms^{-2}Hz^{-1/2} \qquad (1.4)$$

The study of temperature's influence is divided in two subsystems: GRS and OMS.

1.3.1.1. Noise effects inside GRS

Thermal gradient fluctuations cause differential pressures on opposite TM faces which push them away from their real position. This occurs due to three mechanisms: asymmetric out-gassing, radiation pressure and radiometer effect.

1.3.1.2. Noise effects inside OMS

Temperature fluctuations have a relevant effect on the refractive index of optical elements in the optical bench. Several phenomenons particularly including dilation and contractions of optical elements can be caused by thermal changes. In addition, temperature differences precisely affect the capacitance in photo-diodes as they can result in a phase change of the appraised signal.

1.3.2. Temperature measurement subsystem sensitivity requirement

Ensuring temperature stability is a key factor to consider during the mission. To accomplish that purpose, it is necessary to monitor the temperature in different locations of the LTP structure. Temperature fluctuations dominate in the low frequency band below $100\,\mu Hz$. The expected noise level measured in the frequency band of between $10-30\,\mu Hz$ is $50-100\,mK/\sqrt{Hz}$ for the inner core.

The characterisation of these low frequency temperature fluctuations is relevant for LISA since temperature variations are expected to provide a significant limit to the instrument's performance for the lowest frequency bins of the mission. Being the LISA mission still in phase, they are an important asset for the thermal design.

1.4. Motivation and Objectives

1.4.1. Motivation

ESA attempts to build a 2.5 million kilometers long interferometer in space and is moving on to actually building some prototype technologies. Luckily, they already have a head start on some of it, as the LPF mission was already launched in 2015. This mission proved that LISA's general idea which aims to confirm that two satellites could stay in place relative to each other with extreme precision is feasible.

LISA includes a precision diagnostic system in order to monitor the noise disturbances and their contribution to the noise budget. Temperature fluctuations are significant as they dominate in the low frequency regime. Hence, at such time scales they are all-present in the spacecraft and consequently, they are potential threats to the measuring chain. This could lead to temperature induced path length variations in interferometers.The current LETS is expected to provide a solution capable of measuring the low frequency thermal fluctuations and contribute to decorrelate them from real path-length variations due to GWs.

1.4.2. Objectives

Having shortly described the contest and the main functionality of the thermal diagnostic subsystem, the goals of this thesis are now introduced. Thus, the strategy for the research will seek the following targets:

1) Design a measurement set-up for electronic testing purposes

2) Define the temperature coefficient for a LISA electronic prototype.

3) Study the noise projection to determine the level of noise contribution for a detector output

1.5. Structure of the thesis

The thesis conceives the design of a measurement set-up for LISA 's thermal diagnostic subsystem.

- **Chapter 2** provides an introduction of the temperature measurement subsystem and the theoretical noise analysis for LISA electronic prototype.

- **Chapter 3** aims to evaluate the results obtained for two different experiments. The transfer function and the noise projection analysis is conceived.

Finally, the Conclusions section closes the dissertation with an overview of the work and the main results obtained.

This document is complemented by a few appendices to expand technical details.

- Appendix A describes the analog chain board schematic used
- Appendix B outlines a characterization for the Air Thermal Control Unit (ATCU)

CHAPTER 2. TEMPERATURE MEASUREMENT SUBSYSTEM

2.1. State of the art

A broad spectrum of fields in elementary physics advocate for high precision temperature measurements. Actually, such high precision requirements are on demand for high-level stable environments which concede the viability of long term methods regarding experimental procedures. In the majority of cases, the already stated methodologies are distinctive in space missions. Certainly, the number of missions that endeavor to reach such stability is increasing. Chiefly among space missions, the GW detection LISA mission highlights in this specific area in view of facing the challenge of achieving the utmost sensitivity in the milliHertz frequency regime. When ultra-stable operations are considered, prominence must be given to the fact that temperature fluctuations can induce undesired perturbations. These disturbances can alter scientific measurements and lead to path-length variations in interferometers.

As aforementioned, in recent times, the subject of high temperature resolution has evolved among the industries. Hence, the attraction of developing fresh up-to date technologies that sustain this level of performance has also increased. To cite an instance, optical metrology has experimentally reach temperature resolutions of $80\ nK/\sqrt{Hz}$ at $100\ Hz$ as detailed in [19]. Another example is focused on the principle of using nanotechnology to design temperature sensors based on micro-cantilevers which lead to achieving a precision of $10\ \mu K/\sqrt{Hz}$ above $1\ Hz$ as described in [20]. Notwithstanding the new developments, restive-based systems are still the most reliable and long heritage for space missions. The latter present a similar level of performance as the nano techniques. Further to this, the temperature diagnostics subsystem for LPF was a case proof of a high precision at very low frequency with an in-orbit performance of $10\ \mu K/\sqrt{Hz}$ down to $1\ mHz$ whereas the LISA TMS intends to reach a $1\ \mu K/\sqrt{Hz}$.

To design and develop a LISA prototype TMS increasing one order of magnitude performance, an ESA contract was proposed under LETS. This project is based on two main components: the Front-End Electronics (FEE) composed by Analog Front-end Board (AFB), Power Distributing Board (PDB) and Digital Processing Board (DPB) and the ultra-stable test bench composed by aluminium shield layers inside vacuum tank and peltier elements for active control. The current LETS will provide a new solution capable of fulfilling the high requirements for measuring such low frequency temperature fluctuations.

With that in mind, a preliminary design description is provided. The LETS EBB as previously mentioned is divided in three Printed Circuit Board (PCB)s to improve flexibility and reduce the overall design. The PDB presents the electronics responsible to generate the power supply of the other boards. The DPB host a Microcontroller Unit (MCU) which controls the data acquisition process and the communication with an external computer. Finally, yet importantly, the AFB includes the required interfaces to generate stimulus signals and to convert analog to digital signals. In the latter PCB the ADC and Digital-to-Analog Converter (DAC) are introduced.

2.2. Temperature diagnostics subsystem

The coming sections review an enhanced version of TMS used in LPF. However, a first description of the temperature sensors is provided and eventually, an overview of the analog signal processing chains is studied.

2.2.1. Temperature sensors

Allegedly, when small temperature fluctuations are expected to be quantified, two temperature sensors outshine. Both NTC and Resistance Temperature Detector (RTD) are founded in the change of a resistor element under changes of temperature.

2.2.1.1. NTC thermistors (NTCs)

Assertedly, a thermal sensing technology applicable for LISA regarding space and power conditions are NTC thermistors. Hence, the selected read-out front-end is based on NTCs in the Wheatstone bridge configuration.

NTC thermistors are resistors with a negative temperature coefficient, whereby the resistance exhibits a precise and predictable decrease while the temperature increases. The Steinhart-Hart equation (2.1) expresses the resistance-temperature relationship of a thermistor.

$$T^{-1} = A + B \ln R(T) + C \ln^3 R(T) \tag{2.1}$$

T is the temperature in Kelvin units and A, B and C correspond to the constant coefficients given by the manufacturer. Particular relevance should to attached to the fact that these coefficients are different for each and every sensor and also depend on the temperature range to be measured. Howbeit, for the current analysis Eq. (2.1) is used with the following coefficients: $A = 1.0451254110^{-3}$, $B = 2.1620538410^{-4}$ and $C = 7.9428883110^{-8}$.

$$R(T) = R_0 e^{\beta(T^{-1} - T_0^{-1})} \tag{2.2}$$

The β depends on the thermistor and in terms of small temperature ranges is considered to be constant. Typical values are proximate to 3500. R_0 is the thermistor's resistance at a T_0.

The sensitivity is a relevant parameter of the sensor on account of the noise performance of the system. The higher the sensitivity the lower the noise in the measurement. For small temperature changes, the sensitivity of the thermistors is defined as follows:

$$\alpha = \frac{1}{R_0} \frac{dR(T)}{dT} \tag{2.3}$$

2.2.1.2. Resistance temperature detectors (RTDs)

Reportedly, platinum is a metal that manifest a known change of resistance according to temperature changes. RTDs are currently made of the former element owing to the fact that their change of resistance is heavy enough to measure small-scale temperature variations.

The equation that relates resistance and temperature is designated as,

$$R(T) = R_0[1 + \alpha_{Pt}(T - T_0)] \tag{2.4}$$

where α_{Pt} is the sensitivity of the platinum sensor.

It is to be noted that for R_0 values larger of $10\,k\Omega$ the noise performance of the system is not as excellent as one could prefer. Figure 2.1 illustrates the change in the resistance as a function of the temperature for platinum RTDs and for NTC thermistors. As aforementioned, the sensitivity of platinum RTD is not enough to fulfil the demanding requirements of the measurement.

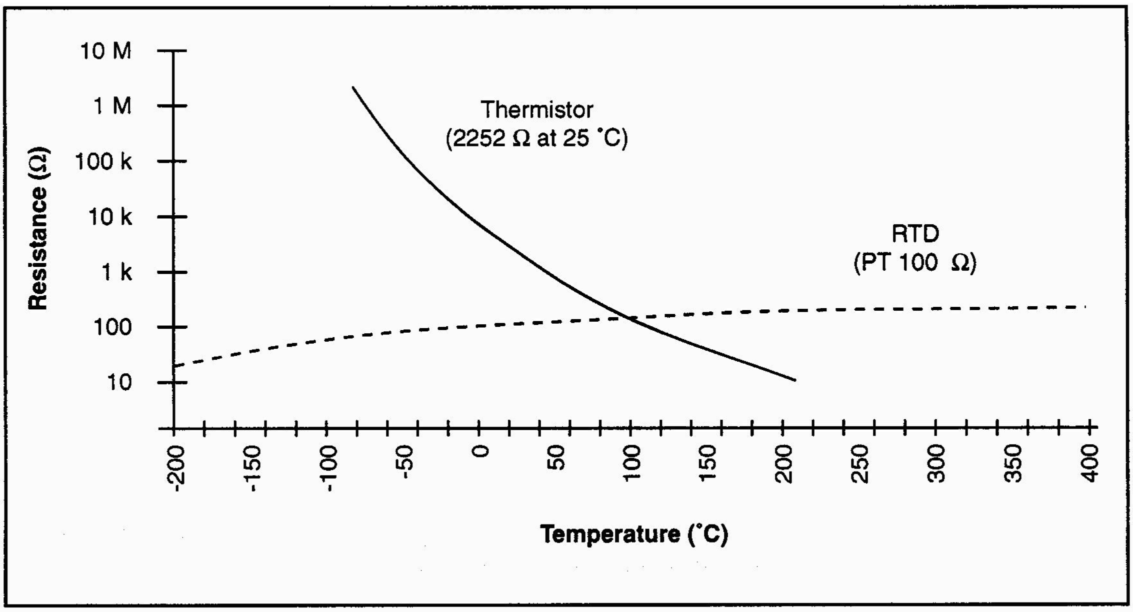

Figure 2.1: Resistance vs. temperature for NTC and RTD [8].

Thereby, NTC will be used to proceed with the experimental measurements.

2.3. Sensor read-out electronics design

First and foremost, as previously mentioned, the selection of the sensor is currently based on the providence of sensitivity requirements. By the same token, the NTC are immune to the expected radiation levels inside the spacecraft. This technology has proven a high reliability performance even though they present magnetic material content and a not negligible power dissipation (down to the hundred of micro-watts).

For the purpose of reading the actual sensor value, the Wheatstone Bridge (WB) configuration is preferred inasmuch as it permits a notable reduction of the noise total contribution by maximizing the gain of the first active stage of the chain. The value of the fixed resistance of the sensing arm resistor divider is close to the nominal value of the thermistor at the center of the measurement scale in a bid of maximizing the sensitivity. Figure 2.2 draws attention to the read-out block diagram design.

Figure 2.2: Read-out block diagram design.

The sensitivity of the system regarding a voltage amplitude modulation for a WB configuration is determined from the derivative of the voltage with respect to the temperature.

The voltage is defined as:

$$V_o = \frac{V_i R_{NTC}(T)}{R + R_{NTC}(T)} \tag{2.5}$$

The sensitivity is determined as:

$$S_{wb} = \frac{dV_o}{dT} = \frac{\beta V_i}{T^2} \frac{R R_{NTC}(T)}{(R + R_{NTC}(T))^2} \tag{2.6}$$

where β is the thermistor temperature coefficient, V_i is the RMS value of the voltage modulation applied on the WB, T is the temperature, R_{NTC} is the temperature dependent resistance of the thermistor and R is the fixed resistor of the sensing arm.

As above-mentioned, the sensor resistance behaviour is not lineal along the temperature measurement range. Thereupon, it stands to reason that the previously introduced Steinhart-Hart equation Eq. (2.1) is used for the current analysis, whereas for the theoretical analysis the exponential equation of the NTC with its β is assumed. The intention of this procedure is focused on the low demanding absolute accuracy requirements for these project which are not far off $\pm 0.1 K$.

From the latter sensitivity expression several subjects of discussion can be extracted:

(i) The sensitivity increases with the applied voltage on the sensor. Thereby, the dissipated power on the sensor and the sensed location disturbances present the same behaviour.

(ii) The sensitivity does not change with the thermistor resistance.

(iii) The higher the β value, the higher the sensitivity.

The NTC thermistors used have a β coefficient of the order of 4200.

2.4. Read-out implementation

The read-out implementation is composed by the elements illustrated in Figure 2.2.

At first glance, the DAC is the first element controlled by a MCU that runs the LETS read-out software and generates the stimulus signal. Both voltage reference of DAC and ADC are the same with the purpose of having a ratiometric system.

From then onwards, there is the Fully Differential Amplifier (FDA) that converts a single-ended signal into a differential one removing any Direct Current (DC) component. Such balanced driving will eventually minimize the DC applied voltage and the common-mode.

Furthermore, the WB is introduced. As named above, the sensor itself goes with it. At the outputs of the WB there is a difference amplification with a fixed gain done by two Operational Amplifier (OA)s, as an input stage of the amplifier. The value of this stage is set to maximum value allowing the temperature range of $50\ K$. This is the case, since the sensor impedance is fairly large.

Afterwards, a FDA is located to guarantee the balanced differential driving of the ADC and the common-mode value needed. It is to be noted that when the outputs of the WB are unbalanced, the output of the difference amplification also remains unbalanced due to the low gain considered in the previous stage. If a FDA with a unitary gain is added, the balance driving of the ADC is recovered and thereby, its full dynamic range is suitable. Distinction must be given to the fact that the added common-mode is only required as the ADC does not present a bipolar analog input.

Finally, yet importantly, the ADC is introduced. Such an element converts this analog value into a digital one and sends it to the MCU.

Table 2.1 outlines the specific components used for the read-out implementation.

Read-out elements	
Digital-to-Analog Converter	AD5781/91
Microcontroller Unit	STM32H745ZI
Operational Amplifier	OPAx189
Fully Differential Amplifier	ADA4945-1
Analog-to-digital converter	ADS1278

Table 2.1: Summary of the components used for the read-out.

In the majority of the cases, for the previous components with the exclusion of the ADC, exist a comparable space component with an insignificantly performance degradation. On the contrary, the selection of the ADC is critical. The main purpose was to build at least a 10 sensor design with a scalable layout, thus if multi-channel high-resolution ADCs are desired, the number of options is scarce. In the end, it was decided to use the ADS1278, which is an 8-channel simultaneous sampling 24-bits resolution ADC.

It is to be noted that all the high stability resistances in the EBB are made of foil compositions with a $0.05\ ppm/K$ thermal coefficients in view of reducing as far as possible the temperature sensitivity of the read-out electronics. Section 2.7. reviews its analysis in further detail. Moreover, the ambition of having a low tolerance to reduce the random uncertainty of the entire system is currently present.

2.5. Principle of measurement

The main purpose of the system design is measuring low magnitude amplitude signals at the low frequency regime. In order to achieve this aim, a modulation signal ought to be generate to locate the sensor response to a higher frequency region with a lower level of noise floor. The nominal frequency for the measurements is desired to be far away from the $1/f$ noise of the amplifier. Its selection is a trade-off between the $1/f$ noise, the bandwidth aimed and the possible effects that may occur due to the wires. Hence, the frequency of interest is around $10\,Hz$.

Further to this, emphasis must be placed on the fact that a square signal modulation is considered for all the results presented in this dissertation. Whether a comparison is assumed regarding the sinusoidal signal, one can conclude that the square signal is immune to the phase noise of the modulation and its computation in the demodulation of the signal coming out from the Instrumentation Amplifier (IA) and the proper low-pass filtering is way more simple.

Finally, yet importantly, the conversion performed to transform the measured voltage to temperature, can be approximated by the following linear expression:

$$T_m = \frac{V_{ADC}}{V_{wb} S_{wb} G} + T_0 \tag{2.7}$$

where T_m is the temperature measured by the system, V_{ADC} is the voltage measured by the ADC, V_{wb} is the Root Mean Square (RMS) voltage applied on the Wheatstone bridge, G is the gain of the full acquisition system, s_{wb} is the sensitivity of the Wheatstone bridge and T_0 is the center temperature offset of the current scale.

The divider of this expression is non-linear for the real case and needs to be calibrated for the whole sensing range. However, as it will be seen in the following sections, this approximation allows us to assess the expected theoretical noise of our measurement system and temperature coefficient of the read-out.

2.6. Theoretical analog chain noise characterization

The most critical elements of the EBB design are the analog chain noise budget and how the ambient temperature fluctuations at the read-out electronics will degrade the system performance. Hence, a preliminary noise analysis is undertaken for the analog chain. Each component's data sheet has been considered during the process.

The analog signal circuit is composed by three relevant blocks: (i) the Wheatstone bridge circuit, (ii) Multiplexor (MUX)s, IA and Low Pass Filter (LPF) stage and (iii) the ADC circuit as previously mentioned.

The elements involved are listed as follows:

i) Thermistor Arm

ii) Reference Arm

iii) Operational Amplifier

iv) Fully Differential Amplifier

v) Analog-to-digital converter

The individual noise contribution concerning each of the forenamed elements is contemplated[1]. It is to be noted that the analyzed circuit board used for the noise analysis is in annex A.

2.6.1. Thermistor arm

The thermistor arm noise is characterized by the thermal noise, following the next equation:

$$S_{sense}^{1/2} = \sqrt{4k_b T R_{eq}} \tag{2.8}$$

where k_b is the Boltzmann constant, T the temperature and R_{eq} the equivalent parallel resistance between the thermistor and the stable resistor.

Assuming a center of scale of $25\ ^\circ C$, for a $30\ k\Omega$ fixed resistor, the noise for this first element is $16\, nV/\sqrt{Hz}$ that easily translates to a noise density of $0.5\, \mu K/\sqrt{Hz}$

2.6.2. Reference arm

The reference arm noise is defined by Eq. (2.8), where the nominal reference arm consists of two $1\ k\Omega$ parallel resistors. Thus, the equivalent resistance is $500\ \Omega$ and the thermal noise at the center of scale is $2.9\, nV/\sqrt{Hz}$ and $0.10\, \mu K/\sqrt{Hz}$.

---

[1] For the noise analysis, all values considered in this section are input referred. They are referred to the sensor itself and converted to temperature with the expression (2.7). For the conversion to temperature noise, the current baseline fixed voltage approach of the Wheatstone bridge supply has been used for calculating the sensitivity.

2.6.3. Operational amplifier

When considering the noise analysis for the two operational amplifiers, both can relate as two voltage followers with a feedback resistance without any relevant change in the total noise of this step. For the feedback resistance, a nominal value of $5\ k\Omega$ is used. Hence, the noise contribution of this stage proceeds as follows:

$$S_{OA}^{1/2} = \sqrt{i_{OA}^2(R_{ref}^2 + R(T)_{sense}^2) + 2e_{OA}^2 + \frac{8k_bTR_f}{G^2}} \tag{2.9}$$

where the i_{OA} and e_{OA} are the current and voltage noise spectral density, R_{ref} is the equivalent fixed resistance of the reference arm, $R(T)_{sense}$ is the equivalent resistance of the thermal sensitive arm at the center of scale and G is the gain of this stage. Since the thermal noise contribution of the feedback resistance is on the output of the amplifiers, it must be divided by the gain of the stage to refer it to the input.

For the $OPAx189$ the current noise density is $165\ fA/\sqrt{Hz}$ and the voltage noise density is $5.2\ nV/\sqrt{Hz}$. The noise at the center of scale is $8.4\ nV/\sqrt{Hz}$ and $0.29\ \mu K/\sqrt{Hz}$.

2.6.4. Fully differential amplifier noise

For the FDA, a gain value of one is assumed. Nevertheless, there is still the need to divide the noise by four[2] as it is referred to the full chain input. Thus, its noise contribution is defined by the following equation (2.10):

$$S_{FDA}^{1/2} = \frac{1}{G}\sqrt{2(i_{FDA}R_{FDA})^2 + (2e_{FDA})^2 + 16k_bTR_{f,FDA}} \tag{2.10}$$

where e_{FDA} and i_{FDA} are the voltage and current noise spectral density of the fully differential amplifier and $R_{f,FDA}$ are the resistors of the feedback and input chain of the FDA.

The current and voltage noise spectral densities are determined by:

$$i_{FDA}^2 = i_0^2(1 + \frac{f_{c,i}}{f}) \tag{2.11}$$

$$e_{FDA}^2 = e_0^2(1 + \frac{f_{c,v}}{f}) \tag{2.12}$$

For the low power mode of $ADA4945-1$, the values are: $e_0 = 7\ nV/\sqrt{Hz}$, $f_{c,v} = 40\ Hz$, $i_0 = 4\ pA/\sqrt{Hz}$, $f_{c,i} = 1\ kHz$. Assuming a stimulus signal of $10\ Hz$ and a scale temperature of $25\ ^\circ C$, the noise contribution results as $4.5\ nV/\sqrt{Hz}$ and $0.15\ \mu K/\sqrt{Hz}$.

---

[2] Gain value of the previous stage.

As outlined in Figure 2.3, the FDA noise depends on the frequency, hence if a comparison with the previously introduced noise contributions is assumed, one can conclude that for low frequency bins the major noise effect will be originated in the FDA.

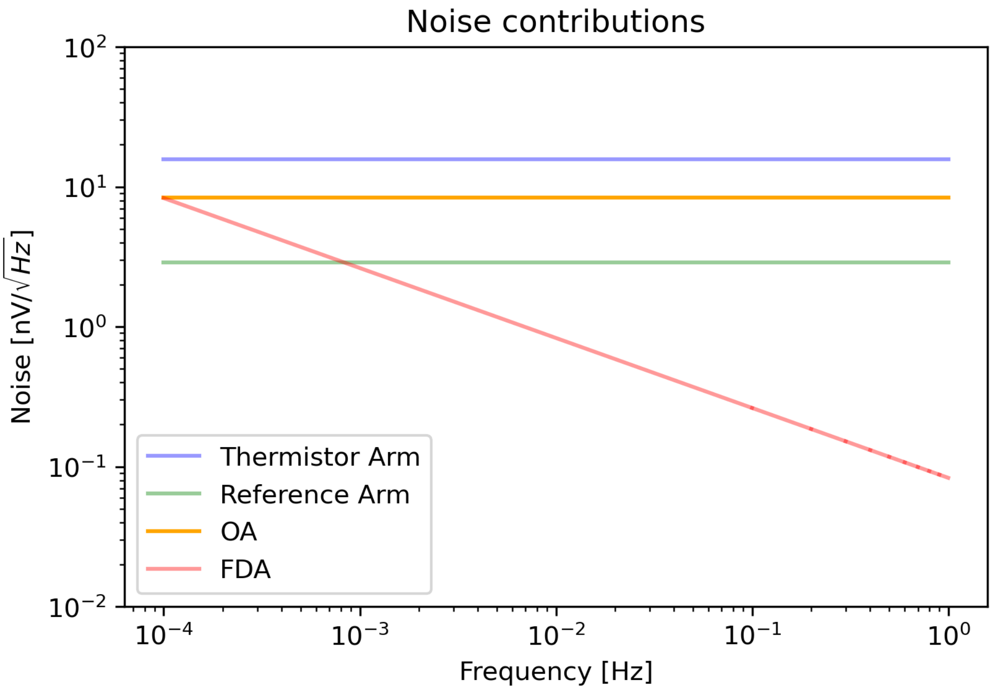

Figure 2.3: Fully Differential Amplifier noise contribution comparison with OA and thermistor and reference arm noise contributions.

2.6.5. Analog to digital converter (ADC)

For the ADC, two sources of noise are distinguished: quantization noise and conversion noise.

2.6.5.1. Quantization noise

Th quantization noise is the intrinsic noise of any digital number due to the finite resolution. For an ideal ADC, the involving noise is expressed as:

$$S_{ADC,q}^{1/2} = \frac{\frac{FSV}{2^{bits}}}{\sqrt{12}} \frac{1}{\sqrt{\frac{f_s}{2}}} \tag{2.13}$$

where Full Scale Voltage (FSV) is input range of the ADC ($5\ V$ for the ADS1278), $bits$ are the number of bits of the ADC (24 bits for the ADS1278) and f_s is the sampling frequency of the ADC ($52734.375\ Hz$ for the maximum sampling frequency of the ADS1278 working in high resolution mode).

The quantization noise is $0.5\ nV/\sqrt{Hz}$ and $0.02\ \mu K/\sqrt{Hz}$.

2.6.5.2. Conversion noise

Conversion noise has its origin in the intrinsic noise of the active components inside the ADC when converting the analog value to a digital. Sigma-Delta ADC have usually a lower conversion noise due to the internal noise shaping, which effectively moves the conversion noise to higher frequencies, outside of the band of interest. Although, some noise always remains.

The $ADS1278$ has an RMS noise in high resolution mode of $5.6\,\mu V\ RMS$. Appearently, if such noise is assumed to be white (uniform spectral density),the following equation can be used:

$$S^{1/2}_{ADC,conv} = \frac{1}{G}\frac{ADC_{RMS}}{\sqrt{\frac{f_s}{2}}} \tag{2.14}$$

The conversion noise is $8.6\,nV/\sqrt{Hz}$ and $0.29\,\mu K/\sqrt{Hz}$.

2.6.5.3. ADC noise

$$S^{1/2}_{ADC} = \sqrt{S^2_{ADC,q} + S^2_{ADC,conv}} \tag{2.15}$$

2.6.6. Total noise contribution

Since the input referred different noise contributions are uncorrelated, the total noise is defined by the square root of the sum of square rule which is expressed as:

$$S^{1/2}_{EBB} = \sqrt{S^2_{sense} + S^2_{ref} + S^2_{OA} + S^2_{FDA} + S^2_{ADC}} \tag{2.16}$$

From here, and using the previous equations of this section, the total noise for a dissipated power of $50\,\mu W$.

Table 2.2 outlines the theoretical noise in the center of scale.

Read-out elements	**Temperature Noise Density [μK/$\sqrt{Hz}$]**	**Contribution on the overall [%]**
Sensor Arm	0.54	57
Reference Arm	0.10	2
Difference Amplification	0.29	18
Fully Differential Amplifier	0.15	4
Analog-to-digital converter	0.29	19

Table 2.2: Summary of the read-out noise contributions.

The total expected noise for EBB $\approx 0.7\,\mu K/\sqrt{Hz}$, hence it is below the required $1\,\mu K/\sqrt{Hz}$.

The result for the contributions in Table 2.2, exposes that the element which provides a major effect is the sensor arm itself. The FDA and ADC noises are quite high by itself. When these noise sources are input referred, their contribution is divided by a factor of 4. Hence, larger gains are expected to reduce their contributions. Prominence must be given to the fact that even though larger gains allow a noise reduction in their contributions, they are slightly significant as they are not the most limiting factor. On the contrary, the thermal sensing range will be lowered, thus, the defined gain value of 4 is a trade-off between the thermal sensing range and the noise.[3]

2.7. Temperature coefficient

It is important to mention that thermal coefficients regarding each of the elements of the analog chain should be considered. Any thermal fluctuations at the acquisition chain will produce also a change in the temperature reading, indistinguishable from any change in the temperature at the sensor placement. It is to be noted that this issue is predominantly due to on-ground testing conditions, as for satellite missions there is a higher thermal stability than in the laboratory. Further to this, two type of errors are perceived: zero error and gain error

2.7.1. Zero error

The zero error is always present, it does not depend on the gain of the system.

Regarding the expression of the voltage difference at the output of the WB, the change at the output of the bridge due to the change of ambient temperature can be estimated as follows [4]:

$$\frac{dV_o}{dT_a} = V_i\left(\frac{\alpha_{R3}R_3R_2 - \alpha_{R2}R_2R_3}{(R_2+R_3)^2} + \frac{\alpha_{R1}R_1R_{NTC}}{(R_1+R_{NTC})^2}\right) \tag{2.17}$$

where α is the temperature coefficient of the thermal stable resistors and is defined as:

$$\alpha_{Ri} = \frac{\frac{dR_i}{dT_a}}{R_i} \tag{2.18}$$

If both thermal coefficients and nominal values of the resistances are comparable, Eq. (2.17) can be simplified as:

$$\alpha_{wb} = \frac{dV_o}{dT_a} = V_i\left(\frac{\alpha_{R1}R_1R_{NTC}}{(R_1+R_{NTC})^2}\right) \tag{2.19}$$

---

[3] For each case,the value of the resistance is the same than the value of the thermistor for the objective centre temperature

[4] Assuming a not varying thermistor resistance

2.7.2. Gain error

Emphasis must be placed on the error related to the thermal drift of the gain of the system. If the system response behaves as a linear function:

$$N_{ADC} = G_{ADC} G_{FDA} G_{OA} s_{wb} (T - T_0) \tag{2.20}$$

where N_{ADC} is the digital output of the system, G_{ADC} the gain of the ADC, G_{FDA} the gain of the FDA, G_{OA} the gain of the OA, s_{wb} the sensitivity of the WB, T the temperature of the sensor and T_0 the center scale of the measurement temperature range.

If the derivative of the output regarding the temperature is performed, it results as the sum of independent derivatives.

$$\begin{aligned}\frac{dN_{ADC}}{dT_{amb}} \approx \frac{dN_{ADC}}{dG_{ADC}} G_{ADC} \alpha_{ADC} + \frac{dN_{ADC}}{dG_{FDA}} G_{FDA} \alpha_{FDA} + \frac{dN_{ADC}}{dG_{OA}} G_{OA} \alpha_{OA} + \frac{dN_{ADC}}{ds_{wb}} s_{wb} \alpha_{s_{wb}} \\ = N_{ADC} \left(\alpha_{ADC} + \alpha_{FDA} + \alpha_{OA} + \alpha_{s_{wb}} \right)\end{aligned} \tag{2.21}$$

The induced noise at the output of the ambient temperature change Eq. (2.21) can be expressed as:

$$\begin{aligned}S_{K,eq}^{1/2} = \frac{\frac{dN_{ADC}}{dT_a}}{\frac{dN_{ADC}}{dT}} S_{K,amb}^{1/2} \cong \frac{N_{ADC} \left(\alpha_{ADC} + \alpha_{FDA} + \alpha_{OA} + \alpha_{s_{wb}} \right)}{\frac{N_{ADC}}{(T - T_0)}} S_{K,amb}^{1/2} \\ = \left(\alpha_{ADC} + \alpha_{FDA} + \alpha_{OA} + \alpha_{s_{wb}} \right) (T - T_0) S_{K,amb}^{1/2}\end{aligned} \tag{2.22}$$

What lies ahead of us is that the thermal fluctuations of the several integrated circuits are correlated. Hence, the gain drift of the full acquisition chain is:

$$\alpha_{gain} = \left(\alpha_{ADC} + \alpha_{FDA} + \alpha_{OA} + \alpha_{s_{wb}} \right) (T - T_0) \tag{2.23}$$

Element of the chain	**Thermal coefficient (ADC_{FSV} ppm/ºC)**
DAC8831	0.05
Ultra-stable resistors	0.05
OPAx189	0.001
ADA4945-1	0.02
ADS1278	1.3

Table 2.3: Thermal drift of the analog chain elements.

First and foremost, since the ADC certainly dominates and the WB configuration provides a common signal attenuated when the difference between two outputs is performed, the stimulus signal chain drift has not been considered in the analysis.

2.7.3. Analysis

Whether the temperature coefficients of each element of the chain are considered, the voltage sampled at the ADC can be written as:

$$V_{ADC}(t) = V_{wb}(t)G(1+\alpha_G \Delta T_a)[\alpha_{wb}\Delta T_a + s_{wb}(T_s - T_0)] \tag{2.24}$$

where α_G is the thermal gain error coefficient, T_a is the ambient temperature at the electronics, α_{wb} is the zero thermal error coefficient, as found in (2.17).

The zero thermal error coefficient for the design is equal to $367\ nV/K$. For the gain error, the dominating component as aforementioned, is the ADC gain drift, that is $1.3\ ppm/K$ [5].

Introducing the previous equation (2.7) and converting the expression in spectral amplitudes, we get:

$$S^{1/2}_{T_m,T_a} = \left(\left(\frac{\alpha^2_{wb}}{s^2_{wb}} + \alpha^2_{ADC}(T_s - T_0)^2 \right) S_{T_a} \right)^{1/2} \tag{2.25}$$

where S_{T_m} are the read-out ambient thermal fluctuations and S_{T_m,T_a} is the measured noise from the ambient temperature.

If the aforementioned considerations are taken into account, the $S^{1/2}_{T_m,T_a}$ value for this design is approximately $23\ \mu K/\sqrt{Hz}$.

The following expression considers the combination between the ambient temperature effects and the read-out noise:

$$S^{1/2}_{T_m}(f) = \left(S_{readout}(f+f_0) + \left(\frac{\alpha^2_{wb}}{s^2_{wb}} + \alpha^2_{ADC}(T_s - T_0)^2 \right) S_{T_a}(f) \right)^{1/2} \tag{2.26}$$

where the $S_{readout}$ is the electronics noise power spectral density shifted by the stimulus signal frequency.

---

[5] The gain error depends on the temperature point being sensed, thus, it turns out to be important when measuring at the edge of large temperature ranges.

2.8. Conclusions

An analysis has been contrived in order to investigate the expected theoretical noise of our measurement system and temperature coefficient of the read-out.

Major findings referred to the data Table 2.2 state that the main contributing element is the sensor arm. Hence, as it is not a very high value, there is still room for improving its noise floor. In order to reduce the noise floor, one can conclude at first sight that increasing the gain of the total chain could be the best course of action to achieve that goal, notwithstanding, such a procedure would decrease the sensing range and it could negatively affect the whole sensor measurement read-out.

With that in mind, particular importance should be attached to the fact that there is a trade-off between several main objectives.

From the theoretical noise analysis, one can report that even though there is a large temperature range to study, the noise requirements are met.

Finally, yet importantly, it is important to mention that any scientific task involves complex sets of problems and contingencies. Bearing that in mind, this thesis presents an empirical analysis of simplifications regarding the theoretical noise analysis. Hence, after considering that the noise contribution of the sensor arm and the gain drift of the ADC dominate over the rest components, the full account of complexity of equations resulted in a considerable reduction. It is fair to highlight that without the aforementioned assumptions, the computation would have taken ages to be accomplished.

CHAPTER 3. FRONT-END ELECTRONICS EXPERIMENTAL AND THERMAL ANALYSIS

Chapter 3 exposes the experimental procedure done for two different environments. Section 3.1. intends to describe the proposed experimental set-up and the required measurements to obtain the temperature coefficient. Moreover, a brief summary of the signal processing definitions needed is provided and a discussion and evaluation of the results obtained is conceived. Further to this, in Section 3.2. the noise projection for a high stable environment is considered.

3.1. Temperature Coefficient

3.1.1. Experiment concept

A set-up is designed in order to achieve a high temperature stability down to $1\ mHz$. Such a design is characterised by the ability to suppress external environmental thermal fluctuations. This capability is defined by the temperature coefficient.

To estimate the temperature coefficient, the following experiment is proposed:

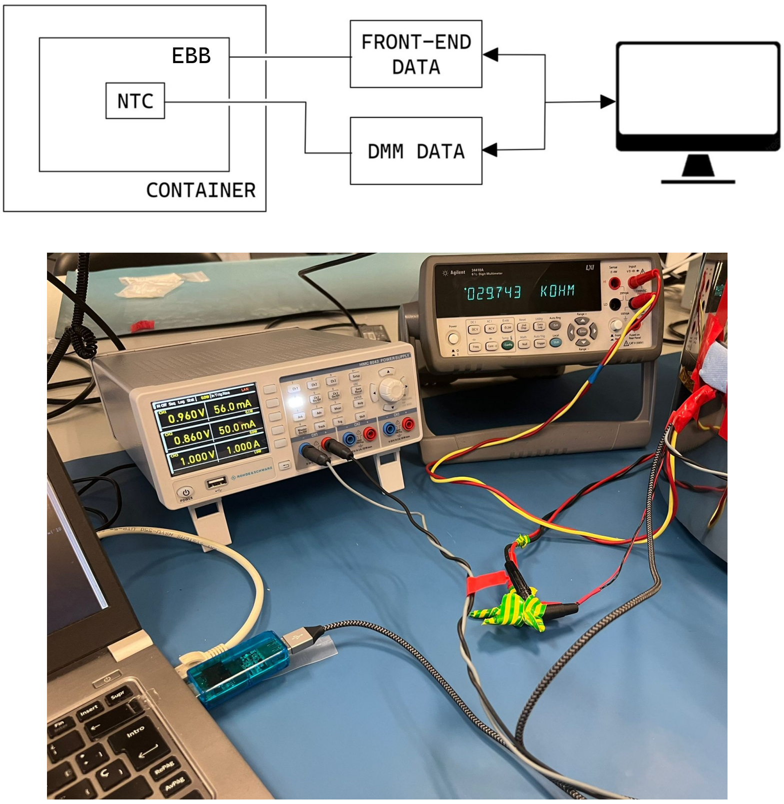

Figure 3.1: Representation of the experiment proposed, being the schematics identified on the top, and the image at the bottom describes the real disposition of the instrumental devices involved in the measurement system.

With the intention of estimating an accurate value of the temperature coefficient, a repetitive sequence of square signals is injected in order to induce a temperature modulation at the output of the system. Such a modulation is measured and highly suppressed by the temperature coefficient of the EBB.

The aforementioned theoretical study proposes a constant value of $23\ ppm/^{\circ}C$ for the analytical temperature coefficient as seen in section 2.7.

If the temperature coefficient is determined, an estimation of the expected temperature fluctuations in the EBB can be provided. For that purpose, there is a projection in Section 3.2. of the NTC data gathered by a DMM in the output of the system using the Transfer Function (TF).

3.1.2. Set-up description

The scheme of the measurement system design is given in Figure 3.2.

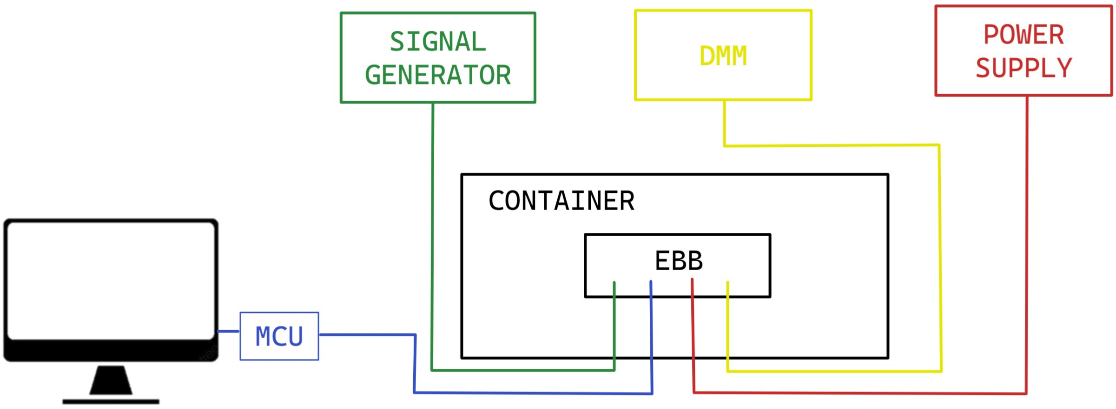

Figure 3.2: Set-up scheme.

At first glance, six components can be distinguished in the previous scheme. The following sections provides a brief description of each part and how they are involved in measurement system.

3.1.2.1. LISA Enhanced Temperature Subsystem Elegant Breadboard

As it stands, the EBB is used for the experimental procedure and as outlined, there is a NTC sensor is attached to it. Thermal grease and insulating tape have been used to get a proper adherence.

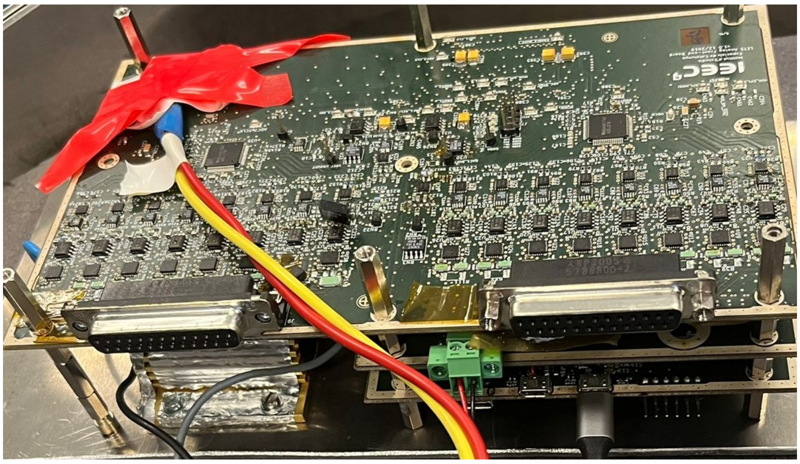

Figure 3.3: Front-end electronics design board used for the experiment.

3.1.2.2. Power supply

Such a EBB is powered by EL302R device as is shown in Figure 3.4 with the following voltage and current values: $28\ V$ and $0.22\ A$.

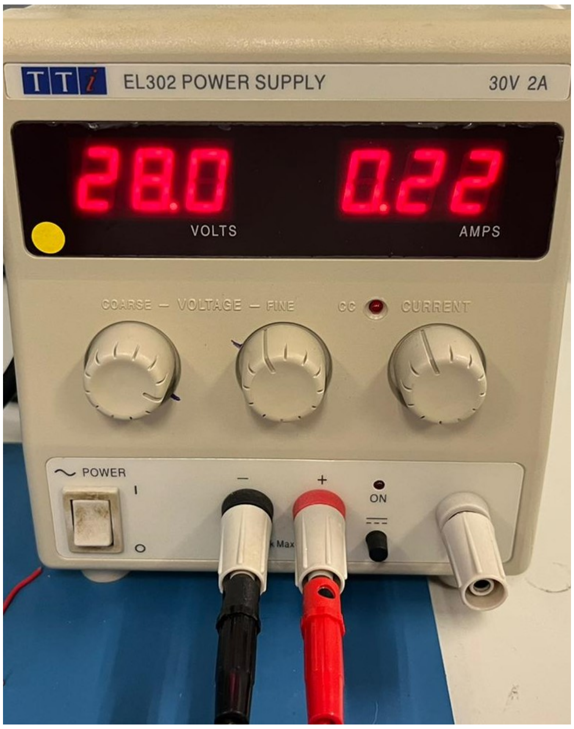

Figure 3.4: Power supply EL302R.

3.1.2.3. Digital multimeter

The NTC sensor used for measuring the temperature fluctuations is connected to the DMM as is shown in Figure 3.2.

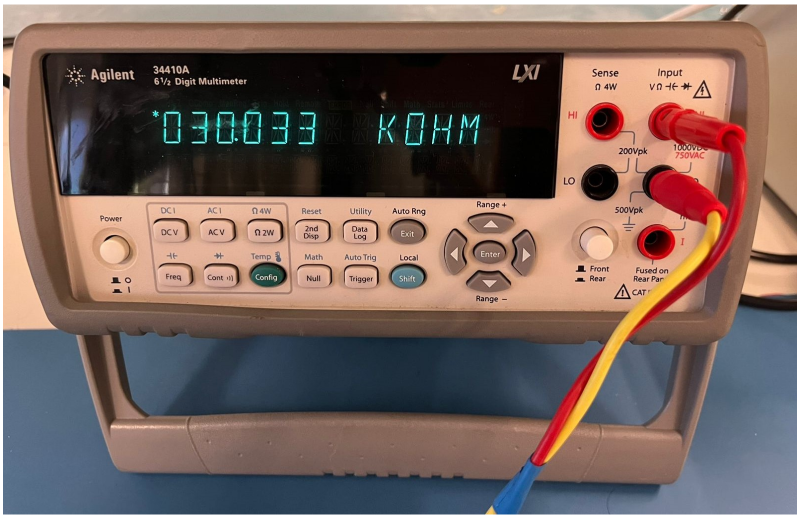

Figure 3.5: Digital Multimeter.

The utility of such a device is focused on gathering the thermal fluctuations in view of the resistance values. The green screen values of resistance will decrease as the temperature inside the container increases. In order to have control over the temperature inside the container to avoid degrading the EBB, the screen values of resistance obtained from the multimeter are constantly being tracked. For the experiment, it has been taken into account that the resistance value is never below of $4.5\ k\Omega$ which is equal to $70\ {}^{\circ}C$ using the Steinhart-Hart coefficients seen in subsubsection 2.2.1.1.

3.1.2.4. Signal Generator

As can be noted, the HMC8043 Power Supply used to generate the desired square signals injections. According to its manual, the power limiting value is set to be $33\ W$ with a maximum output current of $3\ A$ per channel. For this system, only one channel is required as it is illustrated in Figure 3.6. The provided signal is generated by setting a low level voltage to zero and a high level voltage equivalent to the desired power to supply.

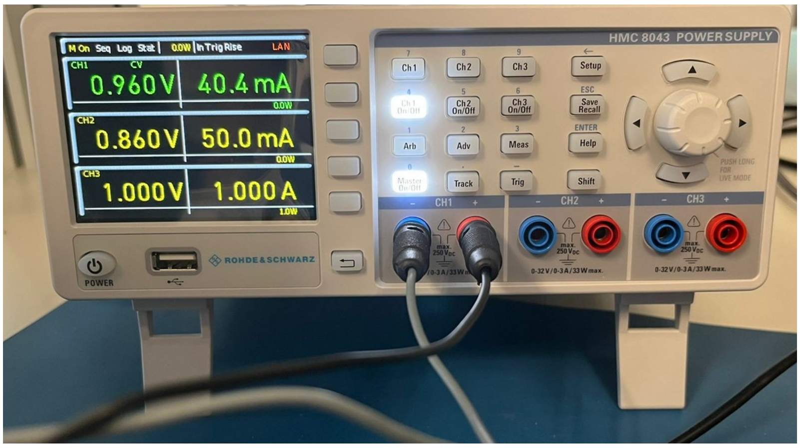

Figure 3.6: Square signal generator used for the experiment.

The gray and black cables are connected to a heater which consists of two resistors of $50\,\Omega$ each in a serial circuit. With the power supplied by this instrument, the resistances are expected to heat up, and afterwards, the temperature inside the container would present a thermal measurable alteration. Such alteration will be used to measure the temperature coefficient of the EBB.

The container proposed for such experimental procedure is shown in Figure 3.7.

Both the EBB and the heater are inside this container in order to keep the thermal fluctuations from going outside.

Figure 3.7: Container used to keep the temperature fluctuations inside.

Figure 3.8 summarizes the components disposition.

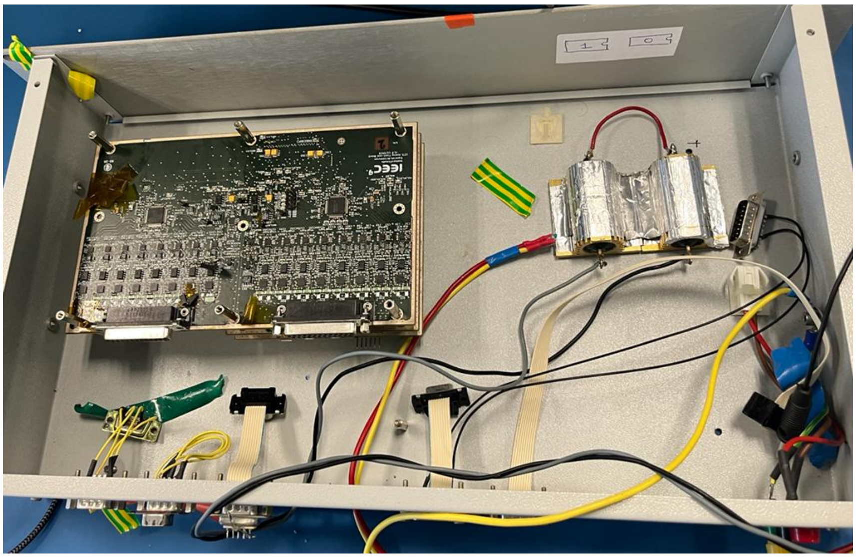

Figure 3.8: Components disposition inside the container.

For the FEE data, there is a cable which connects the EBB with a MCU and consequently, the laptop reads the thermal data from the EBB. The EBB has two ADCs. For the ADC1 channel 0 is enabled, whereas for the ADC2 channels 8, 10 and 12 are considered. The calibration configuration assumed is: channel 0 and 8 are set to $CALREF_{MID}$ whereas channel 10 and 12 are set to $CALREF_{MAX}$. The $CALREF_{MID}$ configuration stands for a balanced WB and the $CALREF_{MAX}$ goes for a maximum unbalanced WB. It is to be noted that the two different configurations will be studied separately.

3.1.2.5. Discussion

To verify the correct functioning of this first set-up, two runs of gathering data have been considered. The earliest one attempts to analyse the unaltered environment case, whilst the latter one perceives the experimental results with a first signal injection at $10\,mHz$. The power supplied is $24\,W$. The following figures show the aforementioned cases.

Figure 3.9 provides some insight over the results for an unaltered environment. As things stands, for the time series graph an upwards tendency is present with apparently random fluctuations nearly the $32.75\,°C$. Such a first transient response is due to the start of the power supply which has not been considered for the following analysis as it could alter the results. Furthermore, given the ASD plot, it depicts a pink noise behaviour where the spectral density increases with decreasing the frequency.

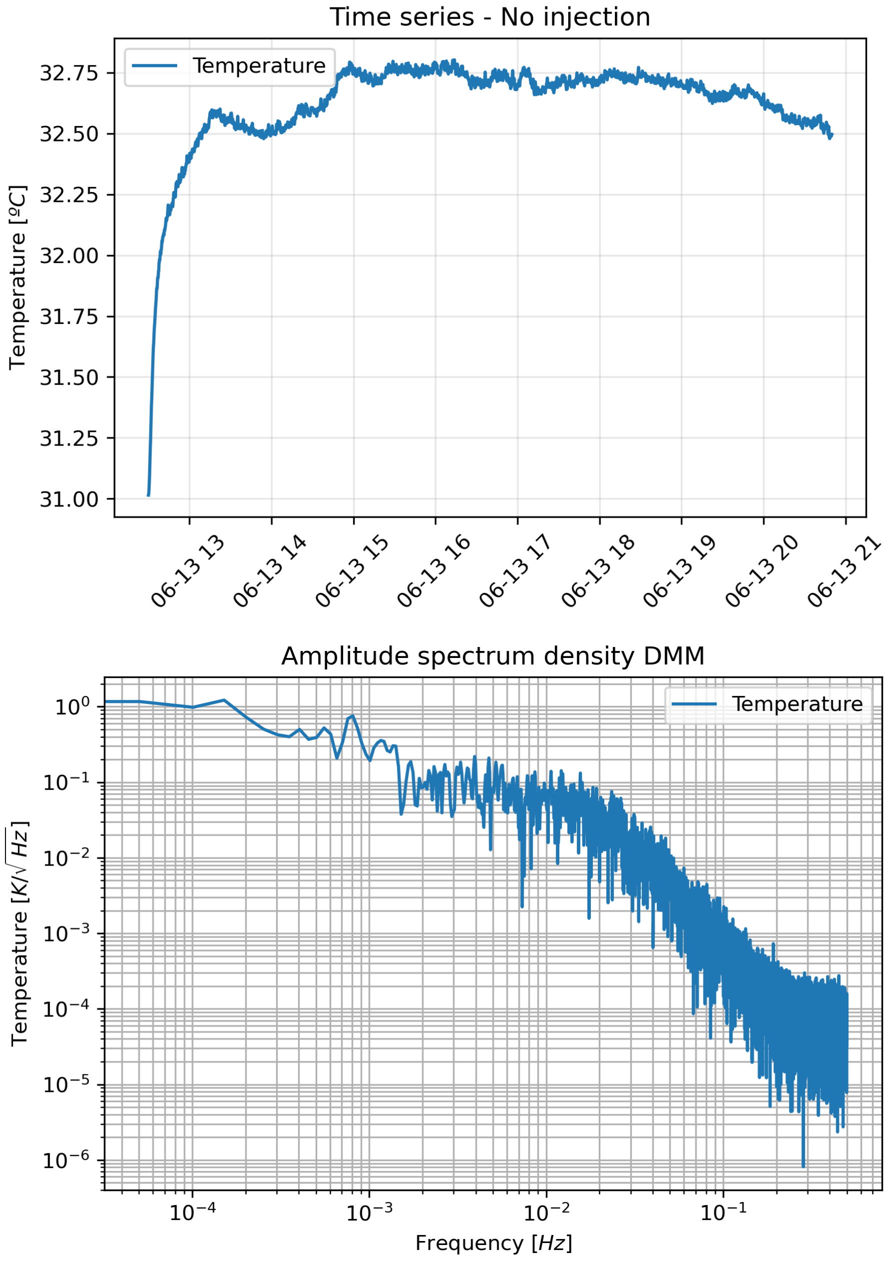

Figure 3.9: Time series and ASD plots for unaltered environment.

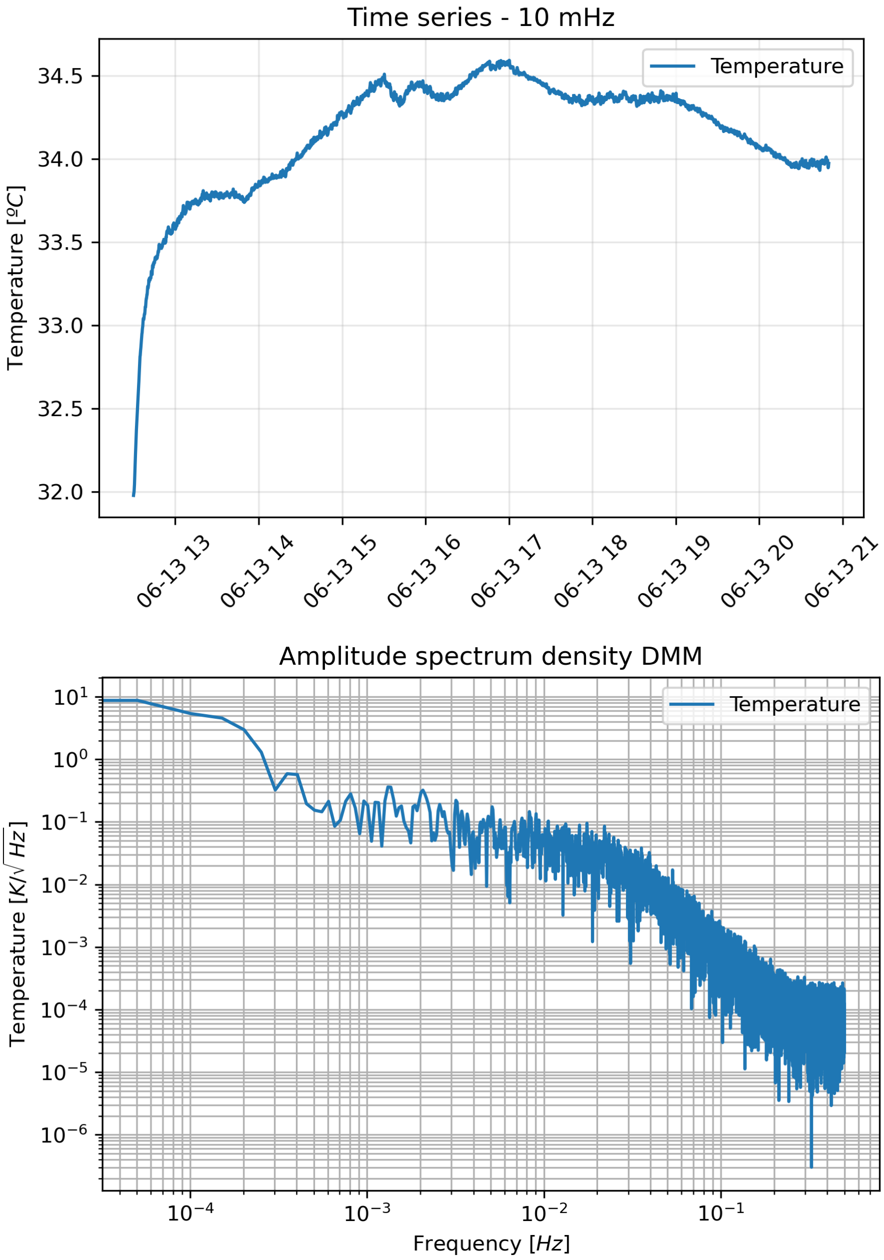

Figure 3.10: Time series and ASD plots for an injection at 10 mHz.

Figure 3.10 exposes a similar behaviour as perceived in Figure 3.9. These results confirm that the system does not witness the injection at $10\,mHz$. If the circuit board was properly being heat up, there should be a relevant visible peak at $10\,mHz$ in the ASD graph. Moreover, an oscillation which should repeat every $100\,s$ does not appear.

Allegedly, the container is poorly keeping the heat inside. With that in mind, we advocate for a finer insulating infrastructure. The new resulting container is described in subsection 3.1.3.

3.1.3. Final set-up description

With the intention of heating up the EBB, a new implemented passive device is proposed. Such a proposition consists of two stainless concentric cylinders that have been mechanized with mirror polished surfaces to suppress heat transfer by radiation.

This container is illustrated in Figure 3.11

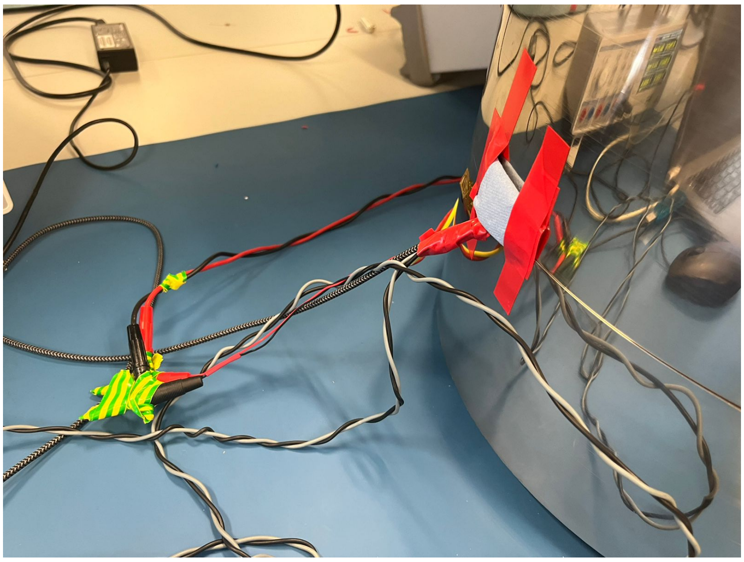

Figure 3.11: Stainless concentric cylinders used to keep the temperature fluctuations inside.

Moreover, in Figure 3.12 one can easily distinguish the final set-up disposition.

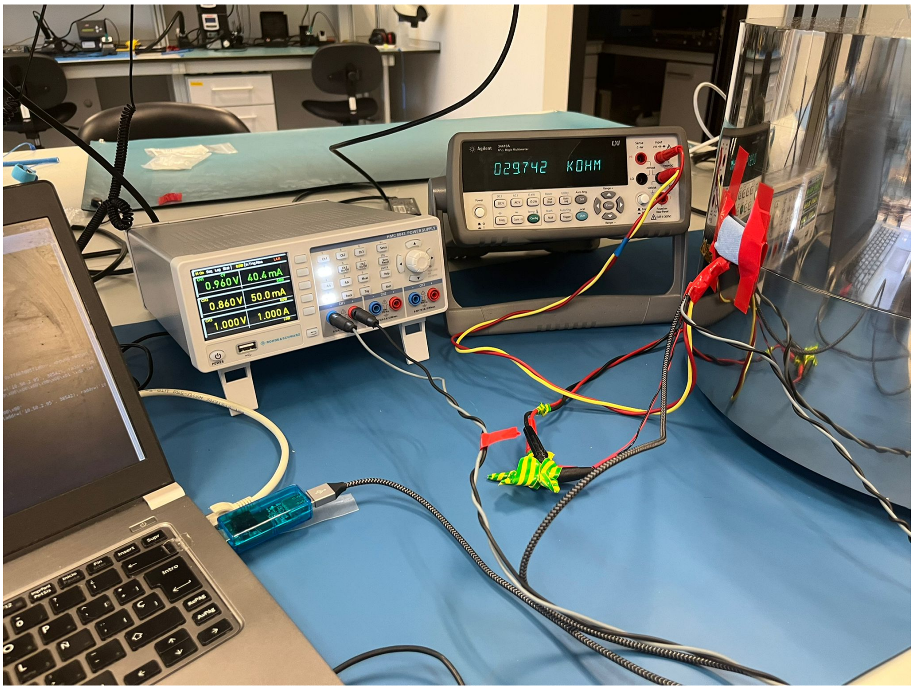

Figure 3.12: Final set-up disposition.

Along with the change of the container, several considerable modifications have been contemplated. To start with, the EBB has been placed on the top of an aluminium plate with screws as can be seen in Figure 3.13. To isolate the EBB from the container's walls, a foam block has been used as support structural basis. Still further, all the cables that go outside the container have been protected with insulating tape to prevent tearing any cable.

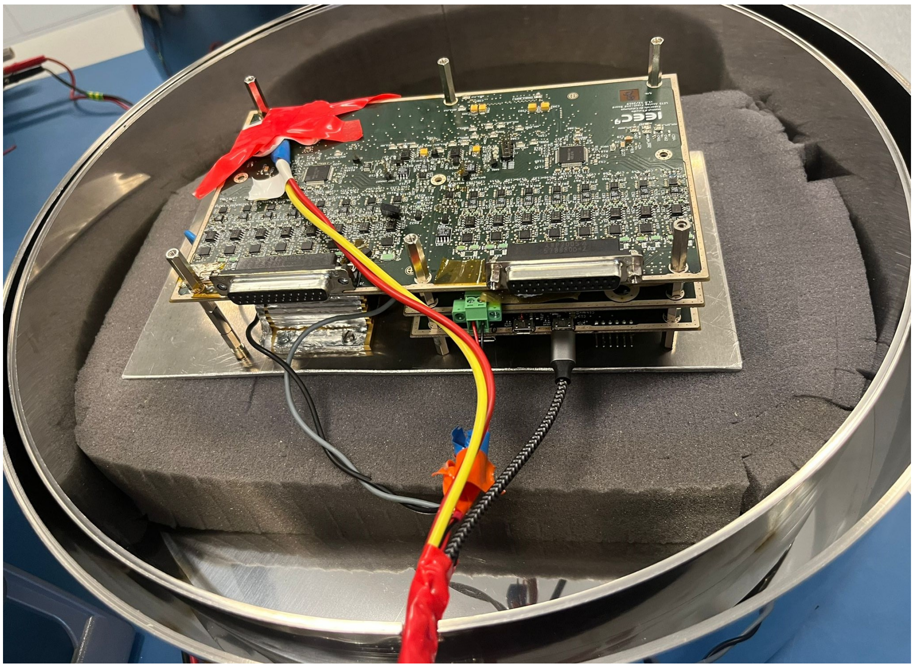

Figure 3.13: Foam block and EBB disposition inside the container

For the purpose to increase the heat transfer from the heater to the electronics, thus increasing the induced temperature fluctuations, two considerations have been stated:

Firstly, the two $50\ \Omega$ resistors haven been disposed in parallel circuit. The equivalent effective resistance value for several resistors in parallel can be computed as the inverse of the sum of the inverses of the resistances according to the following equation:

$$R_{eq} = \frac{1}{\frac{1}{R_1} + \frac{1}{R_2}} \tag{3.1}$$

The equivalent resistance of a parallel will be below the resistances that form the parallel. Hence, considering the following equation:

$$P = \frac{V^2}{R} \tag{3.2}$$

where the P is the effective power consumed by the heater, V is the voltage supplied and R is the equivalent effective resistance of the heater.

If Eq. 3.2 is considered, it can be seen that the power supplied increases as the resistance decreases. With that in mind, if the effective resistance is lower than in the previous set-up, the amount of dissipated power for the save voltage is larger than before. Hence, accordingly to what has been previously mentioned, it provides the alternative to inject a greater amount of power in case it is insufficient to perceive the peak injection in the plots.

Further to this, the location of the heater has changed. Both resistors have been placed under the EBB with the intention of increasing the heat that receives the EBB. As the heater makes contact with the plate, the aluminum plate heats up and the structural supporters from the EBB that make contact with the plate assist on spreading the heat along the circuit board.

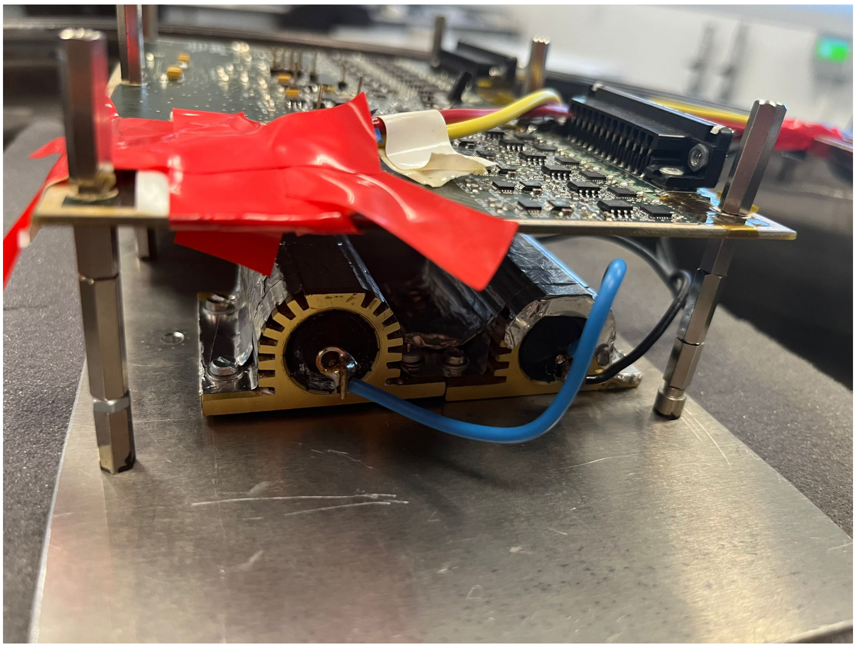

Figure 3.14: Heater disposition composed by two $50\,\Omega$ resistors in parallel

Having considered the aforementioned modifications, several tests have proceed in order to validate its correct functioning. This section aims to verify the proper functioning of the final set-up.

3.1.3.1. Discussion

Figure 3.15, brings evidence about how suitable have the changes been in order to provide a correct performance of the set-up.

For this case, an injection at $1\,mHz$ is applied with a power supply of $24\,W$. The time series plot sheds some light on the present oscillation every $1000\,s$ along the run. To proceed with the ASD analysis, a time series without the transient upwards trend is considered. In addition, the existence of the peak at $1\,mHz$ in the ASD graph, confirms the correct functioning of the new set-up.

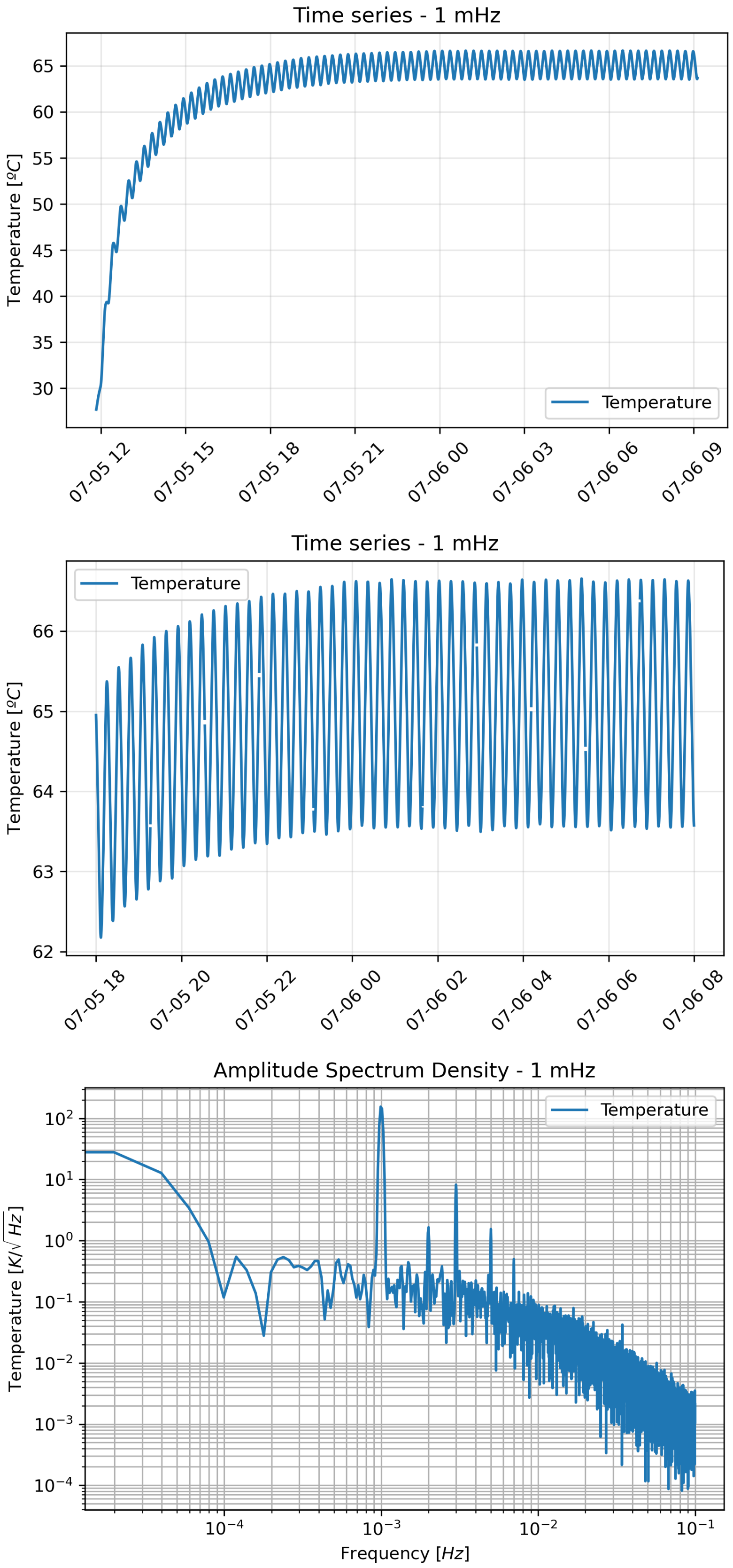

Figure 3.15: Time series and ASD plots for an injection at 1 mHz inside the container. The channel named 'Temperature' describes the temperature data of the EBB, measured by the DMM. From the top to the bottom, the first plot represents the temperature of the he injection, the second is a zoom of the first one, and the third plot exposes the ASD

3.1.4. Data analysis techniques

This section reviews a brief introduction of the basic signal processing definitions needed for the data processing procedure.

Broadly speaking, the experimental data gathered in this thesis could easily be described as a set of q measured temperature time series, $T_i(t)$, i = 1...q that pass through q systems and come together to generate a single measured output $\Phi(t)$. The latter, will present a noise contribution which is considered a random process $n(t)$. If further assumptions such as perceiving the q systems as linear systems proceed, this can be translated into a system of equations in frequency domain:

$$\Phi(\omega) = \sum_{i=1}^{q} H_{T_i\Phi}(\omega)T_i(\omega) + n(\omega) \tag{3.3}$$

where $\Phi(\omega)$, $T_i(\omega)$ and $n(\omega)$ are the Fourier transforms of the inputs, output and noise contribution, and $H_{T_i\Phi}(\omega)$ is the system TF.

The TF is estimated from real data by [21] is defined as follows:

$$H_{T_i\Phi}(\omega) = \frac{S_{T_i\Phi}(\omega)}{S_{T_iT_i}(\omega)} \tag{3.4}$$

where the $S_{T_i\Phi}(\omega)$ and $S_{T_iT_i}(\omega)$ are the Cross Power Spectral Density (CPSD) and the Power Spectrum Density (PSD), which are defined as the Fourier transform of the correlation functions. The aforementioned signal processing definitions as it stands in [22] are explained in further detail in the following sections.

3.1.4.1. Autocorrelation Function

The auto-correlation function $R_{xx}(\tau)$ of a quantity $x(t)$ is the average of the product of the quantity at time t with the quantity at time $(t+\tau)$ for an appropriate averaging time T:

$$R_{xx}(\tau) = \frac{1}{T}\int_0^T x(t)x(t+\tau)dt \tag{3.5}$$

The delay τ can be either positive or negative. For an ergodic process, should approach infinity, but, in practice, T must be finite. The total mean square values x^2 can be estimated by:

$$\bar{x^2} = R_{xx}(0) = \frac{1}{T}\int_0^T x^2(t)dt \tag{3.6}$$

3.1.4.2. Power spectral density

The PSD function $G_{xx}(f)$ by finite Fourier Transform (FT) techniques is defined for $0 < f < \infty$ as:

$$G_{xx}(f) = \frac{2}{T} E\left[|X(f,T)|^2\right] \tag{3.7}$$

where E is the ensemble average, for a fixed f over n_d available samples of $|X(f,T)|^2$. The quantity of $|X(f,T)|$ is a finite FT of $x(t)$ of length T. For $f < 0$ the quanitity $G_{xx}(f) = 0$.

For theoretical studies, a two-sided auto-spectral density function $S_{xx}(f)$ can be defined for $|\infty < f < \infty$ by setting $S_{xx}(f) = \frac{1}{2}G_{xx}(f)$ when $f > 0$ and $S_{xx}(-f) = S_{xx}(f)$. For stationary random data, the $G_{xx}(f)$ is twice the FT of the auto-correlation function $R_{xx}(\tau)$ seen in Eq. 3.5 The total mean square value x^2 can be obtained by integrating $G_{xx}(f)$ or $S_{xx}(f)$ as:

$$\bar{x^2} = \int_0^T G_{xx}(f))df = \int_{-\infty}^{\infty} S_{xx}(f)df \tag{3.8}$$

3.1.4.3. Cross-Correlation Function

The cross-correlation function $R_{xy}(\tau)$ of two quantities $x(t)$ and $y(t)$ is the average of the product of $x(t)$ at time t with the quantity $y(t)$ at time $(t+\tau)$ for an appropriate averaging time T:

$$R_{xy}(\tau) = \frac{1}{T}\int_0^T x(t)y(t+\tau)dt \tag{3.9}$$

For a pair of ergodic processes, should approach infinity, but, in practice, T must be finite. The auto-correlation function $R_{xx}(\tau)$ is a special case of $R_{xy}(\tau)$ when $x(t) = y(t)$.

3.1.4.4. Cross power spectral density

The cross-spectral density function is defined by finite FT techniques for $0 < f < \infty$ as:

$$G_{xy}(f) = \frac{2}{T} E\left[X^*(f,T)Y(f,T)\right] \tag{3.10}$$

where E is the ensemble average, for a fixed f over n_d available associated pairs of $X^*(f,T)$ and $Y(f,T)$ computed from sample records of $x(t)$ and $y(t)$, each of length T. The quantity $X^*(f,T)$ is the complex conjugate of finite FT $X(f,T)$ of $x(t)$, while $Y(f,T)$ is the finite FT of $y(t)$. For $f < 0$ the quanitity $G_{xy}(f) = 0$.

For theoretical studies, a two-sided cross-spectral density function $S_{xy}(f)$ can be defined for $|\infty < f < \infty$ by setting $S_{xy}(f) = \frac{1}{2}G_{xy}(f)$ when $f > 0$ and $S_{xy}(-f) = S^*_{xy}(f)$. For stationary random data, the $G_{xy}(f)$ is twice the FT of the cross-correlation function $R_{xy}(\tau)$ seen in Eq. 3.9.

3.1.5. Experimental Results

Once the system is validated, the next step is to determine the temperature electronics noise contribution by estimating the TF. The subsequent section describes the results obtained for several cases of study. For the succeeding experimental procedures we will be aiming for amplitude variations. Hence, the ASD is considered which is $ASD = \sqrt{PSD}$. as it has proven to be highly useful to see noise limitations.

3.1.5.1. Results for 1, 2 and 5 mHz injections

The following figures feed us with information about how do the system react when a high signal alteration is inserted. Particular attention should be give to the channel named 'Temperature' which describes the temperature data of the EBB, measured by the DMM. For all the following cases, from the top to the bottom, the first plot represents the temperature of the EBB, the second one is a zoom in of the first figure and the third plot represents the ASD for the corresponding injection. Further to this, a power supply of $24\,W$ is considered for all the cases.

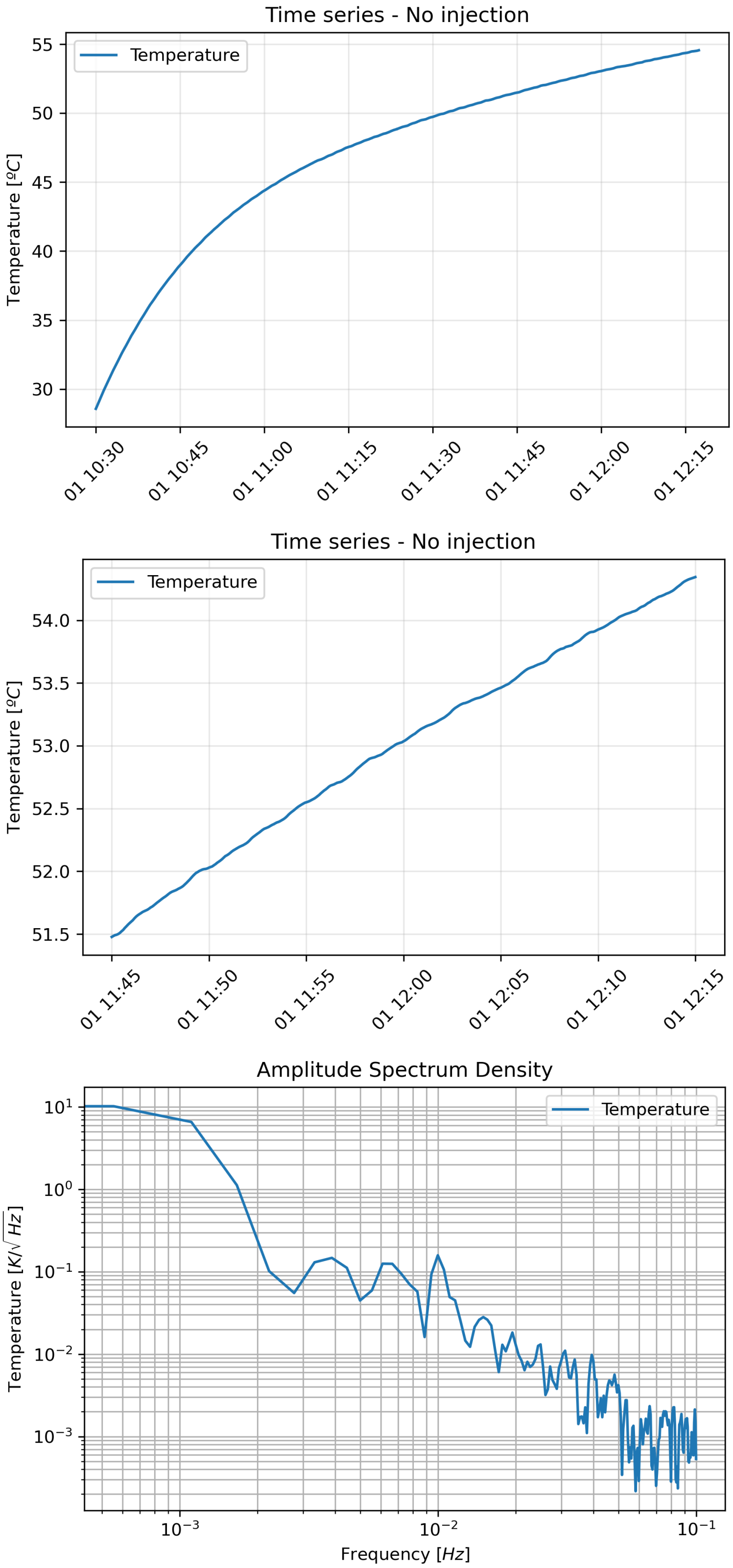

Figure 3.16: Time series and ASD plots for non-altered environment inside the container. The channel named 'Temperature' describes the temperature data of the EBB, measured by the DMM. From the top to the bottom, the first plot represents the temperature of the EBB, the second one is a zoom in of the first figure and the third plot represents the ASD for a non-injection case

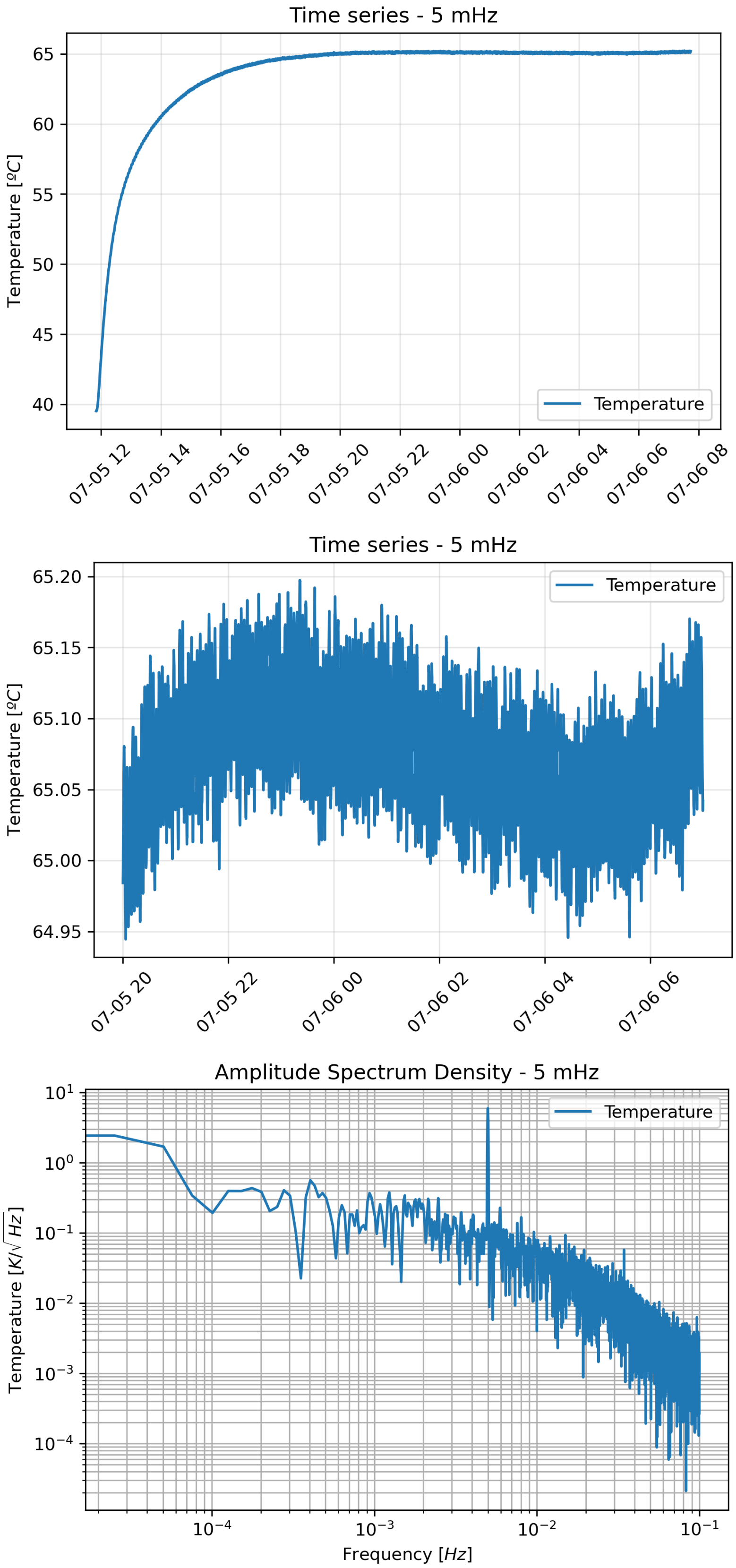

Figure 3.17: Time series and ASD plots for an injection at 5 mHz inside the container. The channel named 'Temperature' describes the temperature data of the EBB, measured by the DMM. From the top to the bottom, the first plot represents the temperature of the EBB, the second one is a zoom in of the first figure and the third plot represents the ASD for an injection at 5 mHz .

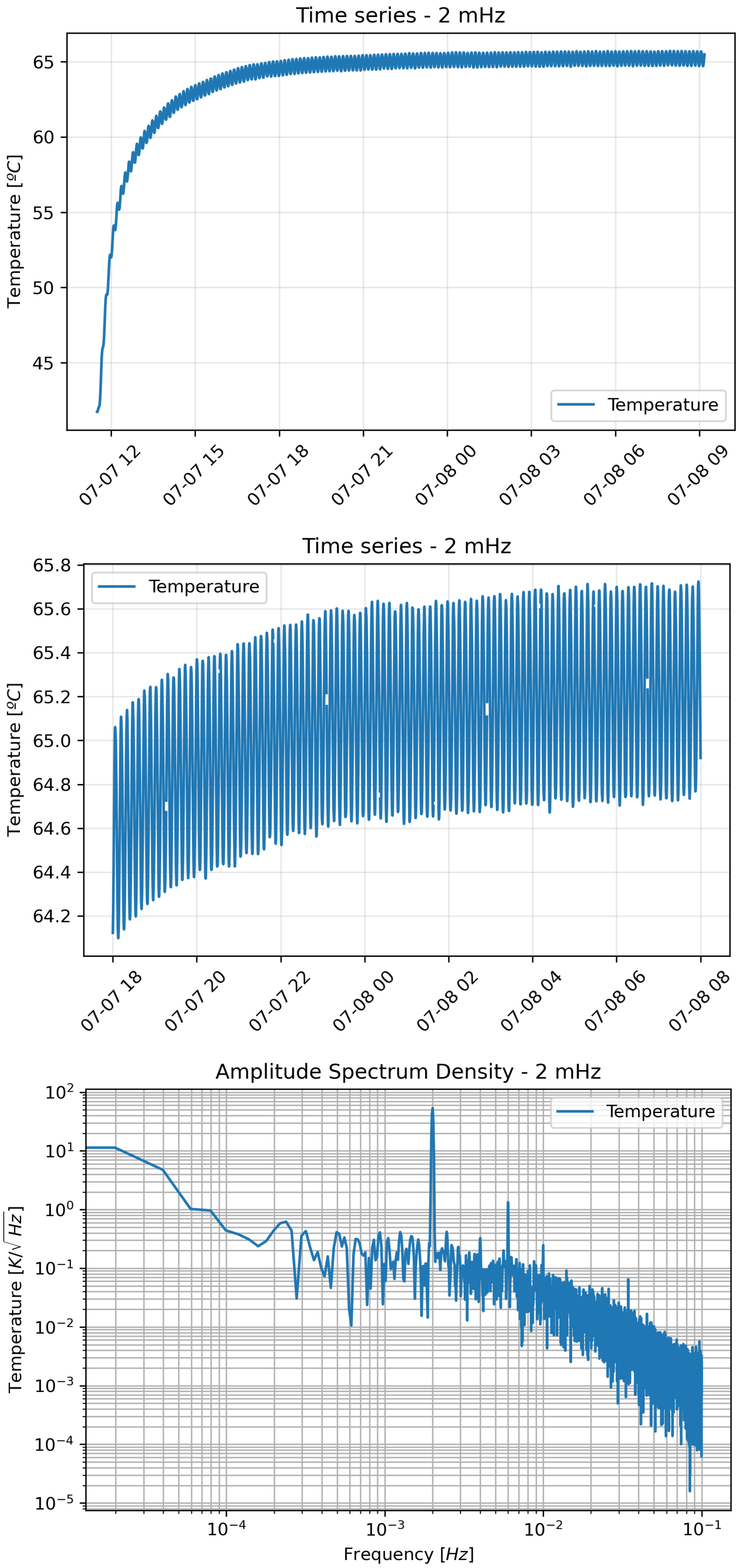

Figure 3.18: Time series and ASD plots for an injection at 2 mHz inside the container. The channel named 'Temperature' describes the temperature data of the EBB, measured by the DMM. From the top to the bottom, the first plot represents the temperature of the EBB, the second one is a zoom in of the first figure and the third plot represents the ASD for an injection at 2 mHz

It is readily apparent that the time series plots give us a clue over the signal injection inserted. As the frequency goes down, the sinusoidal visible fluctuation becomes slower. Allegedly, the amplitude of the fluctuation increases due to the long heating time applied that increases as going down in the frequency regime. For the ASD plots, the peak at the corresponding frequency is present.

Further to this, the times series obtained from the high stability resistances in the EBB is shown in Figure 3.19. As aforementioned, channels 0 and 8 stand for a balanced WB whereas channels 10 and 12 go for an unbalanced WB configuration. Such a fact is clearly observed in the time series FEE plot in voltage units. The voltage value for the balanced channels is zero, whilst the unbalanced ones present a value around of $-0.37\ V$. The conversion from voltage to temperature units is done by using Eq. 2.7. These values can be measured after considering the temperature coefficient of the EBB.

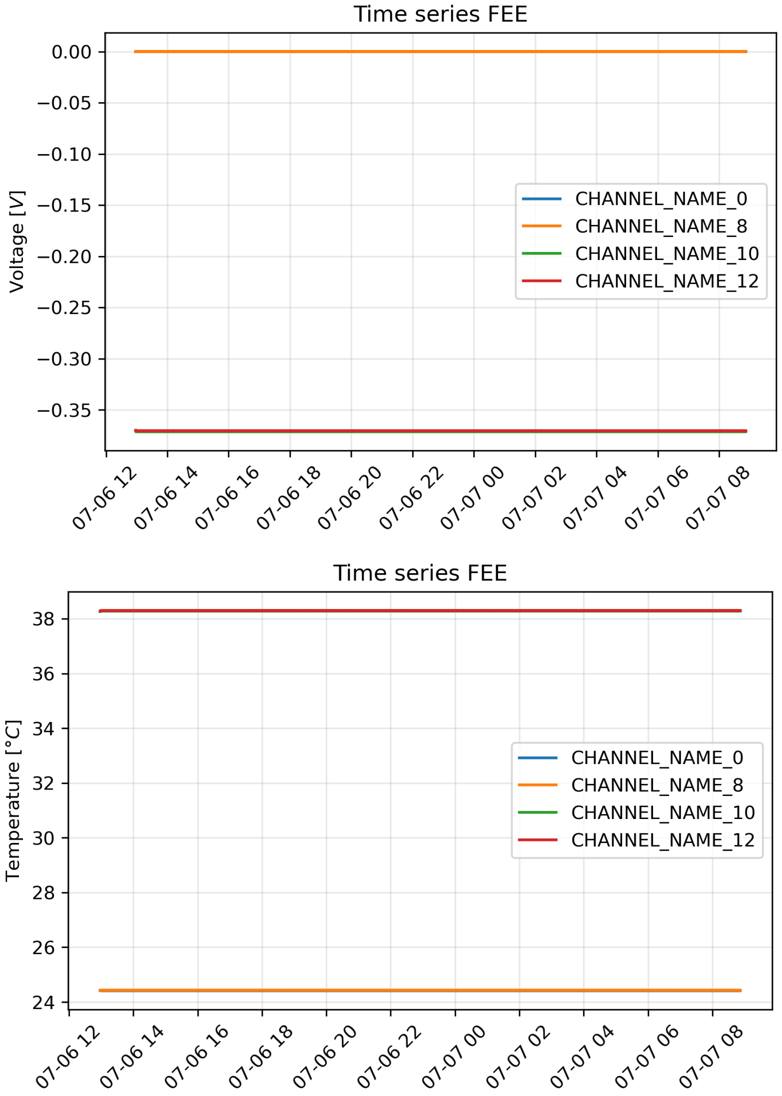

Figure 3.19: Time series of the the high stability resistances in the EBB in voltage and temperature units.

Moreover, it is paramount to highlight the scale difference between the amplitude of temperature of the EBB and the one perceived by the DMM.

Figures 3.20 and 3.21 exposes for the case of $1\ mHz$, the time series comparison for the different channels. It is to be noted that the fluctuations of the EBB is around $1\ mK$. Such a high resolution is required for LISA's mission environment. Furthermore, it is to be noted that with a balanced WB configuration a higher accuracy is achieved than with the unbalanced one.

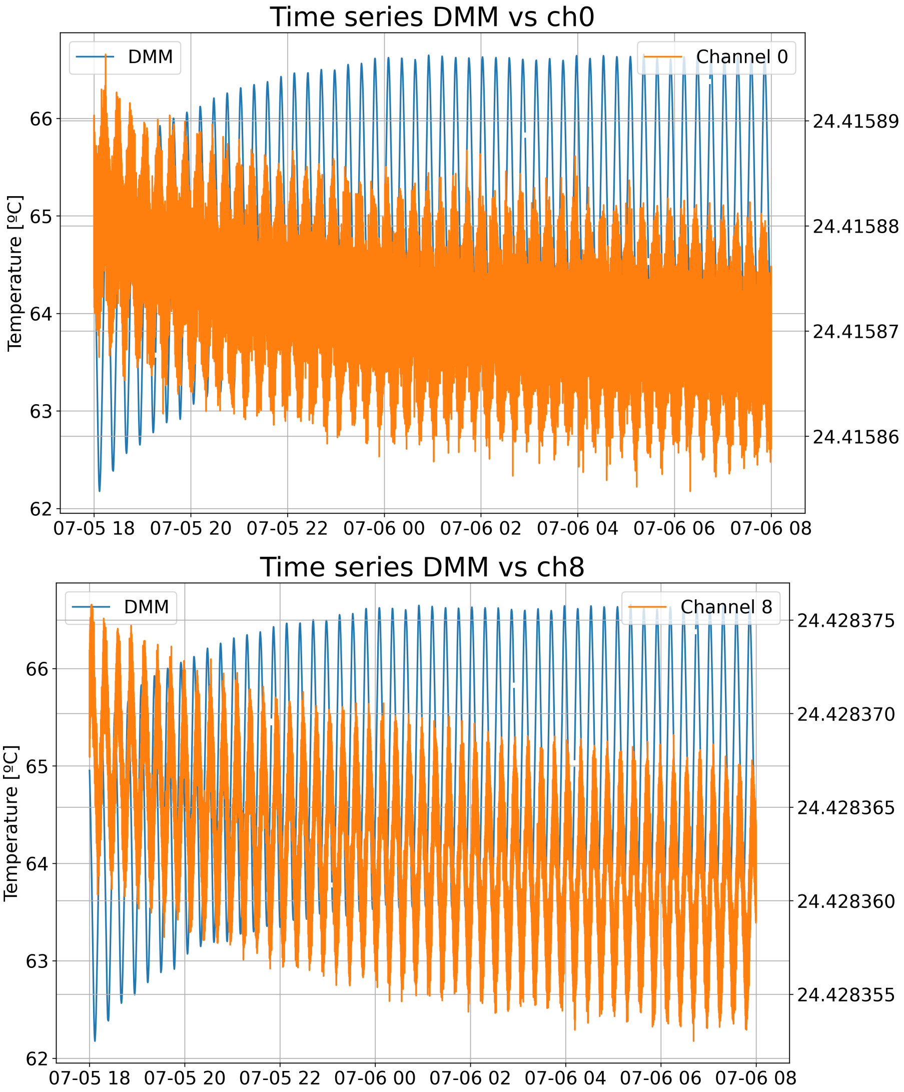

Figure 3.20: Comparison between time series plots for channels 0 and 8 with a balanced WB configuration

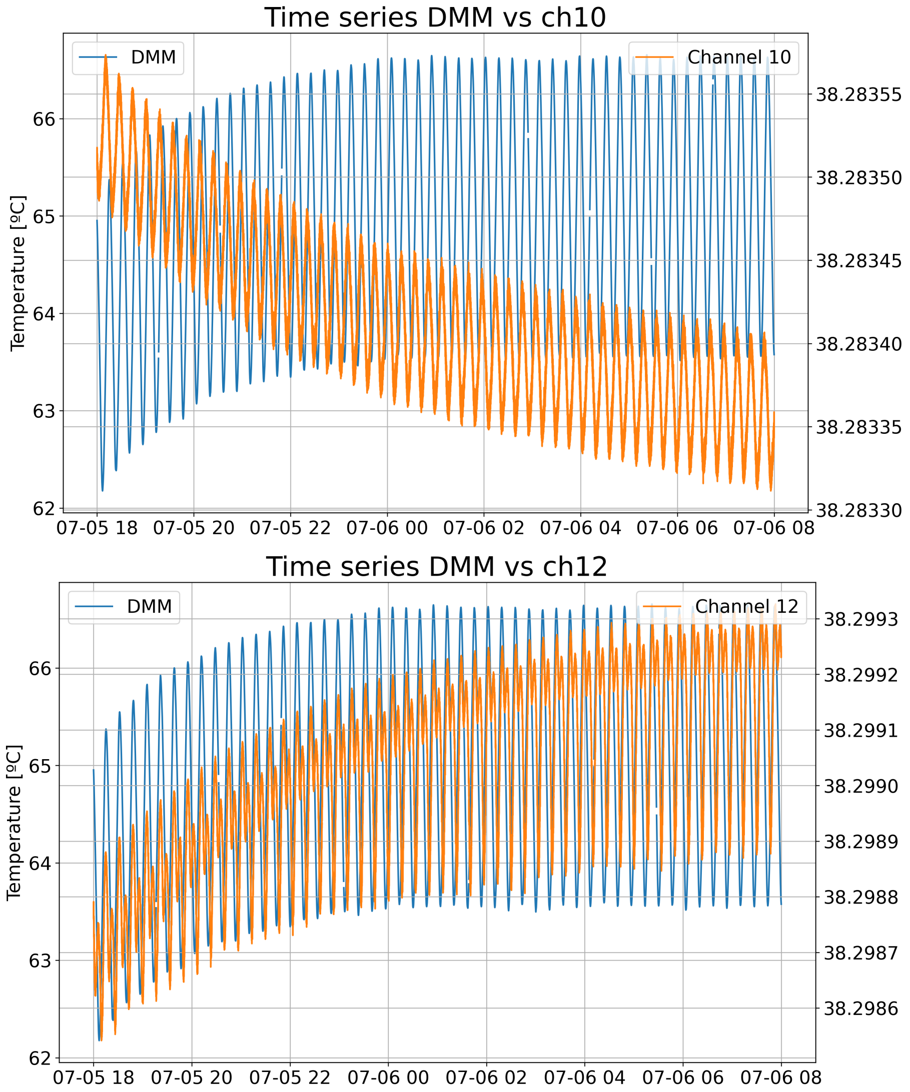

Figure 3.21: Comparison between time series plots for channels 10 and 12 with an unbalanced WB configuration

From then onwards, the equivalent ASD plot for each case is represented in Figure 3.22. As outlined, the corresponding peaks exist and several harmonics appear following the expression: $f_n = nf$ where $n = 1, 2, 3...$ due to square signal injection. In addition, particular importance should be drawn to the fact that there is a slightly difference between the noise levels for the channels. The least noisy is the channel 8 as shown in Figure 3.22.

3.1.5.2. LISA frequency band approach

A particular interesting frequency band to study is the LISA which goes down to $0.1\ mHz$. Hence, to get a proper approach and avoid overheating the EBB, the power supply has been carefully chosen.

A first estimation of the trend that follows the growth of the amplitude of the fluctuations as the frequency increases is conceived.

Firstly, a comparison of the amplitudes is perceived as shown in Figure 3.23.

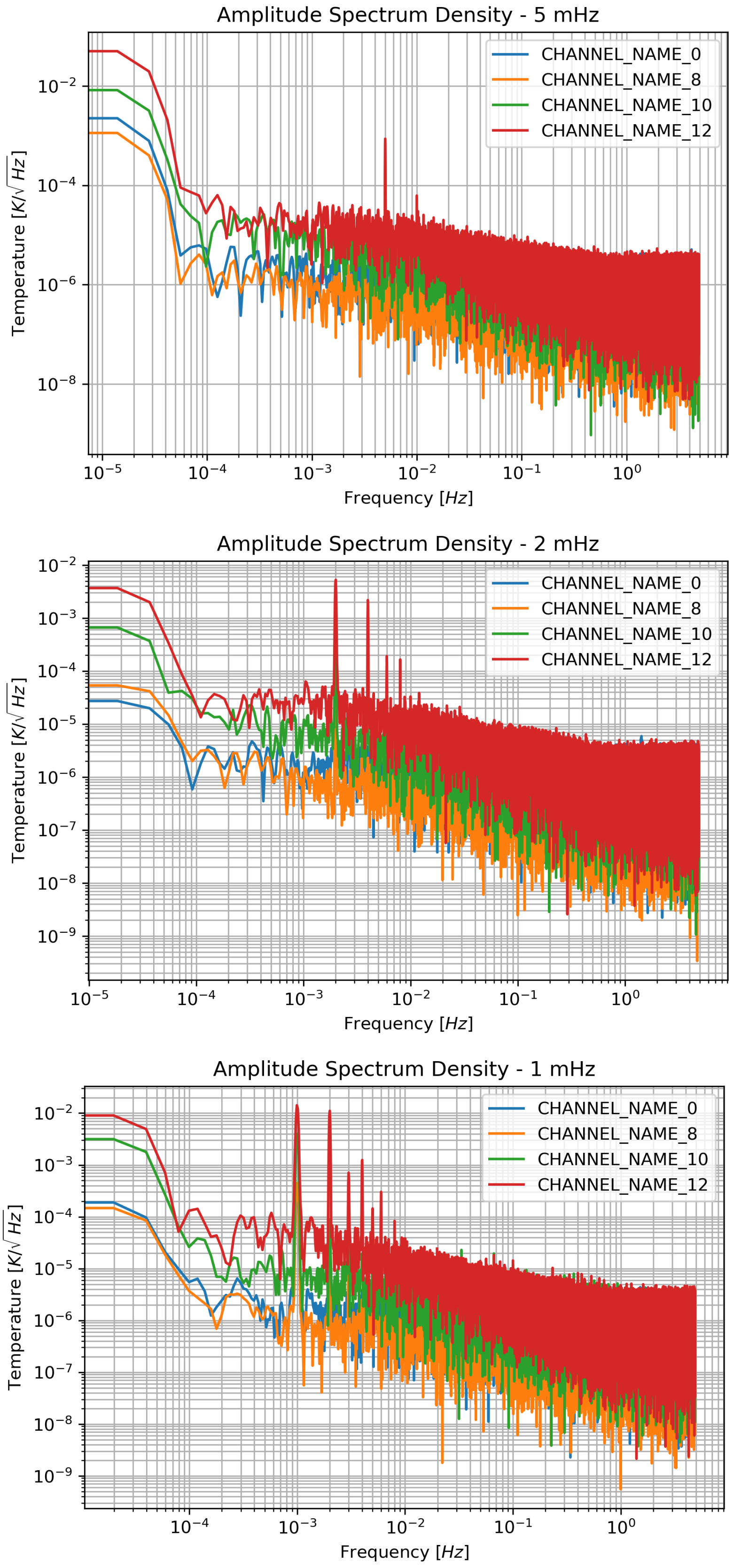

Figure 3.22: ASD plots from the electronics response for 5 mHz, 2 mHz and 1 mHz from top to the bottom .

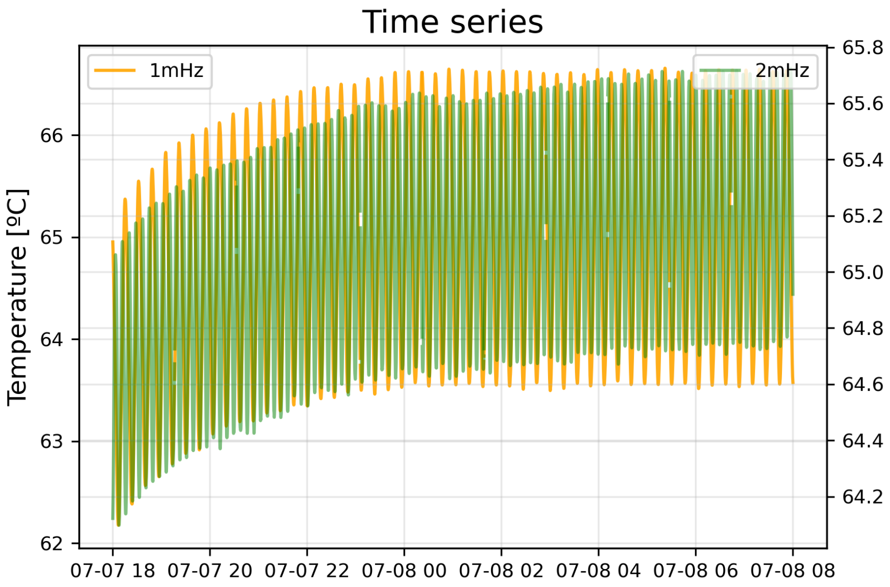

Figure 3.23: Time series plots for 1 mHz and 2 mHz inside the container.

Table 3.1 collects the amplitude results obtained for a 24 W power supply.

Frequency [mHz]	Amplitude [ºC]
5	0.15
2	1.0
1	3.0

Table 3.1: Amplitude values for the fluctuations at several injections.

Having considered the worst case scenario where the amplitude tends to increase linearly, a first estimation of the power supply is $5\ W$ which is expected to result in an peak to peak amplitude of 7°C for a $0.1\ mHz$ injection.

As $5\ W$ is a conservative value, it has been decided to slightly increase the power supply to $8\ W$. Furthermore, along with the DMM device limitations, where the maximum number of counts is up to 50000, the f_s is changed from $5\ s$ to $10\ s$ in order to gather enough data to plot the spectrum. Figure 3.24 shows the results obtained for $0.5\ mHz$ and Figure 3.25 the ones for $0.1\ mHz$.

As it stands, the expected amplitude is obtained and none of them overheats to start degrading the EBB. The temperature top limit is preserved. Figure 3.26 exposes the ASD plot for the latter cases. Once more, the peaks are visible where they should be.

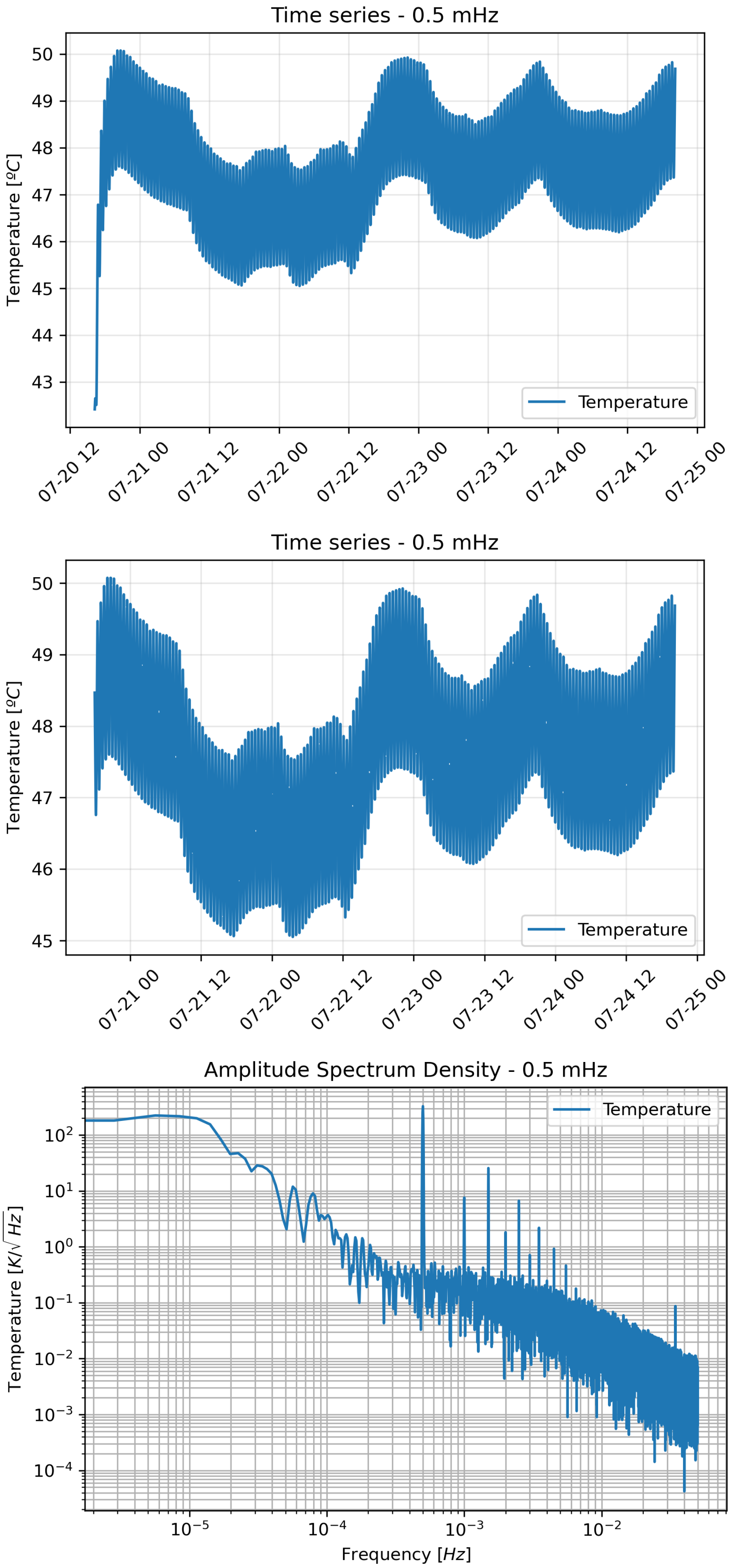

Figure 3.24: Times series and ASD plots for 0.5 mHz inside the container. The channel named 'Temperature' describes the temperature data of the EBB, measured by the DMM. From the top to the bottom, the first plot represents the temperature of the EBB, the second one is a zoom in of the first figure and the third plot represents the ASD for an injection at 0.5 mHz

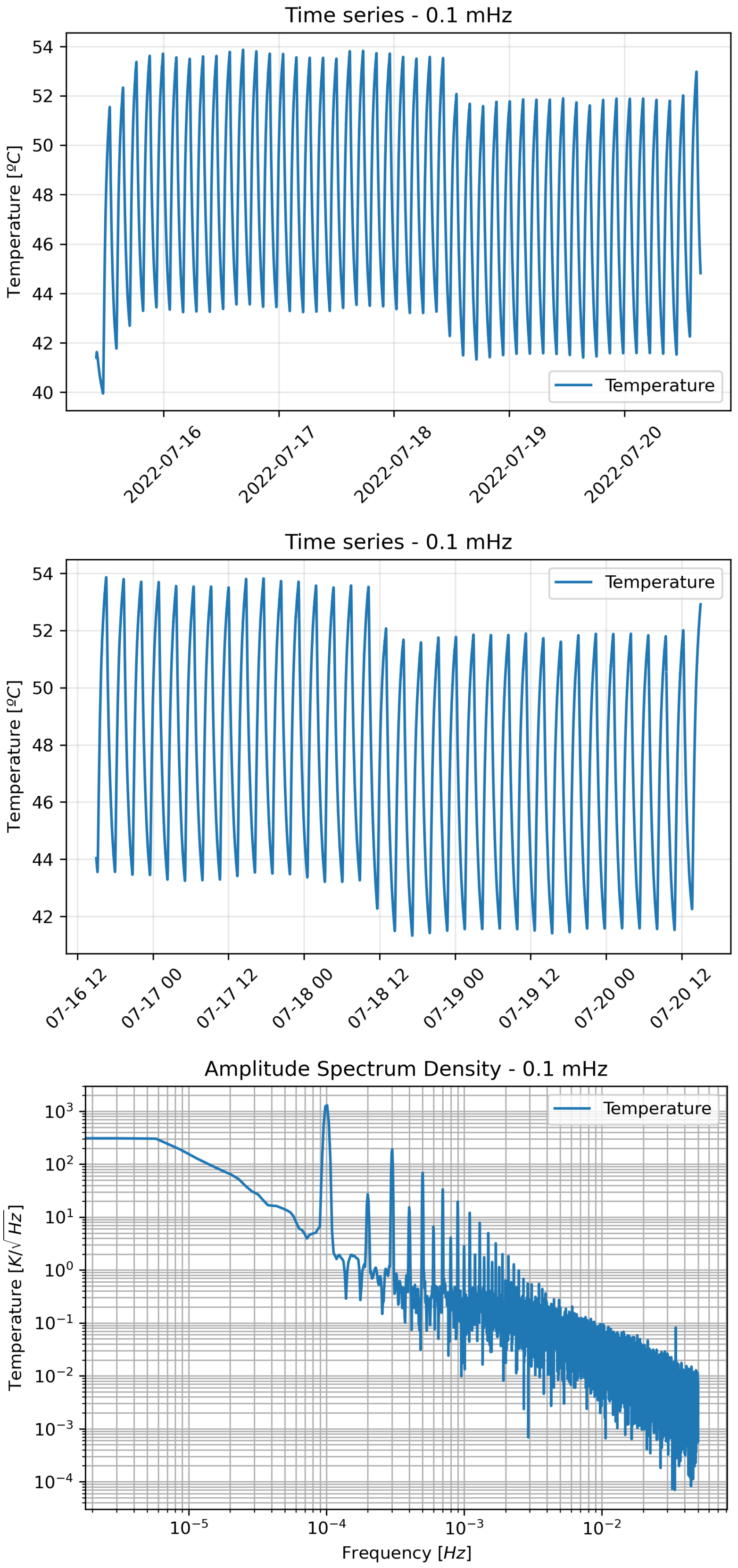

Figure 3.25: Times series and ASD plots for 0.1 mHz inside the container. The channel named 'Temperature' describes the temperature data of the EBB, measured by the DMM. From the top to the bottom, the first plot represents the temperature of the EBB, the second one is a zoom in of the first figure and the third plot represents the ASD for an injection at 0.1 mHz

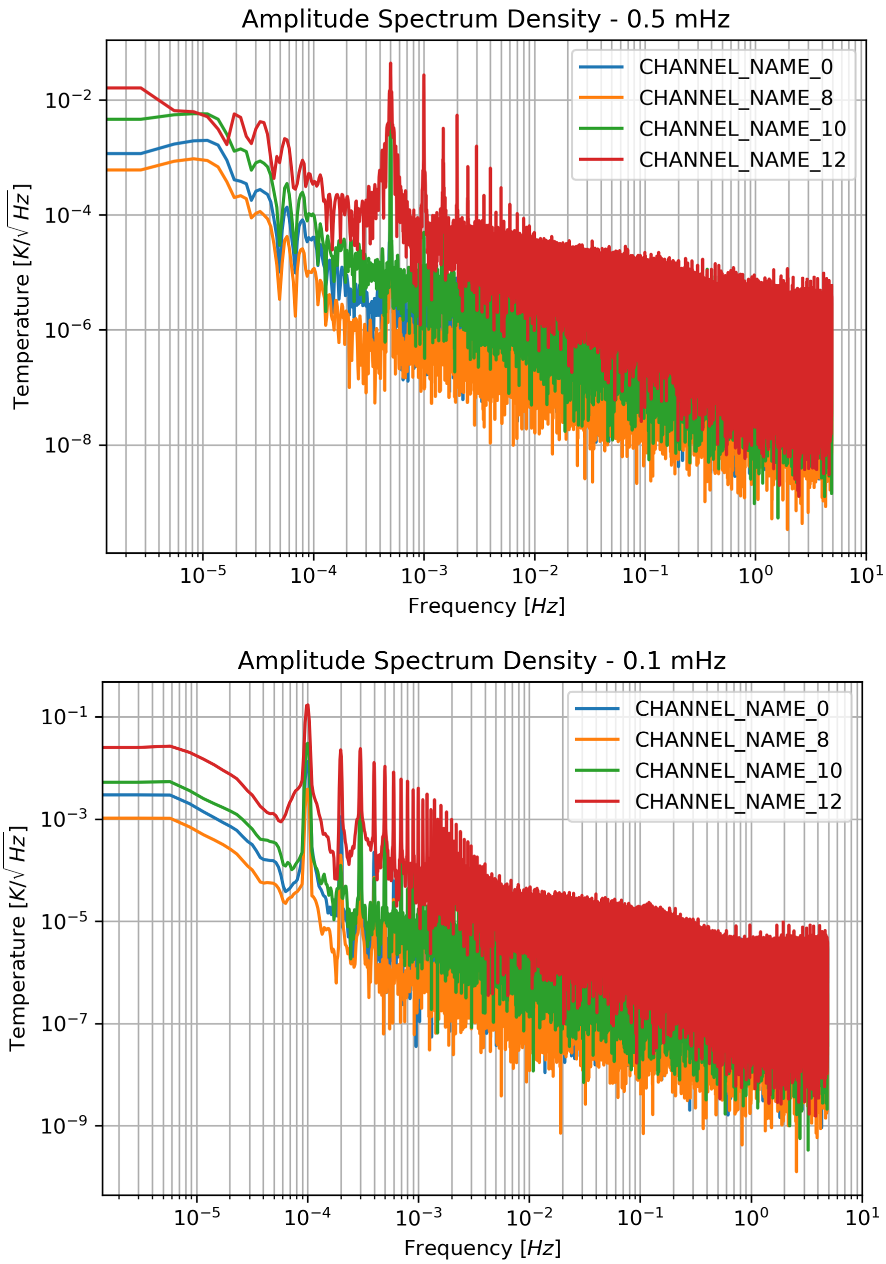

Figure 3.26: The high stability resistors in the EBB ASD plots for 0.5 mHz and 0.1 mHz.

3.1.5.3. Temperature coefficient

This section depicts the results of the TF obtained for the aforementioned cases. Figure 3.27 aims to expose the TF obtained by each channel and for each case. Emphasis must be placed on the fact that two different estimations of the TF have been carried out. One with a balanced WB and another with an unbalanced WB.

Figure 3.27 describes the TF results obtained for the several injections within the balanced WB configuration.

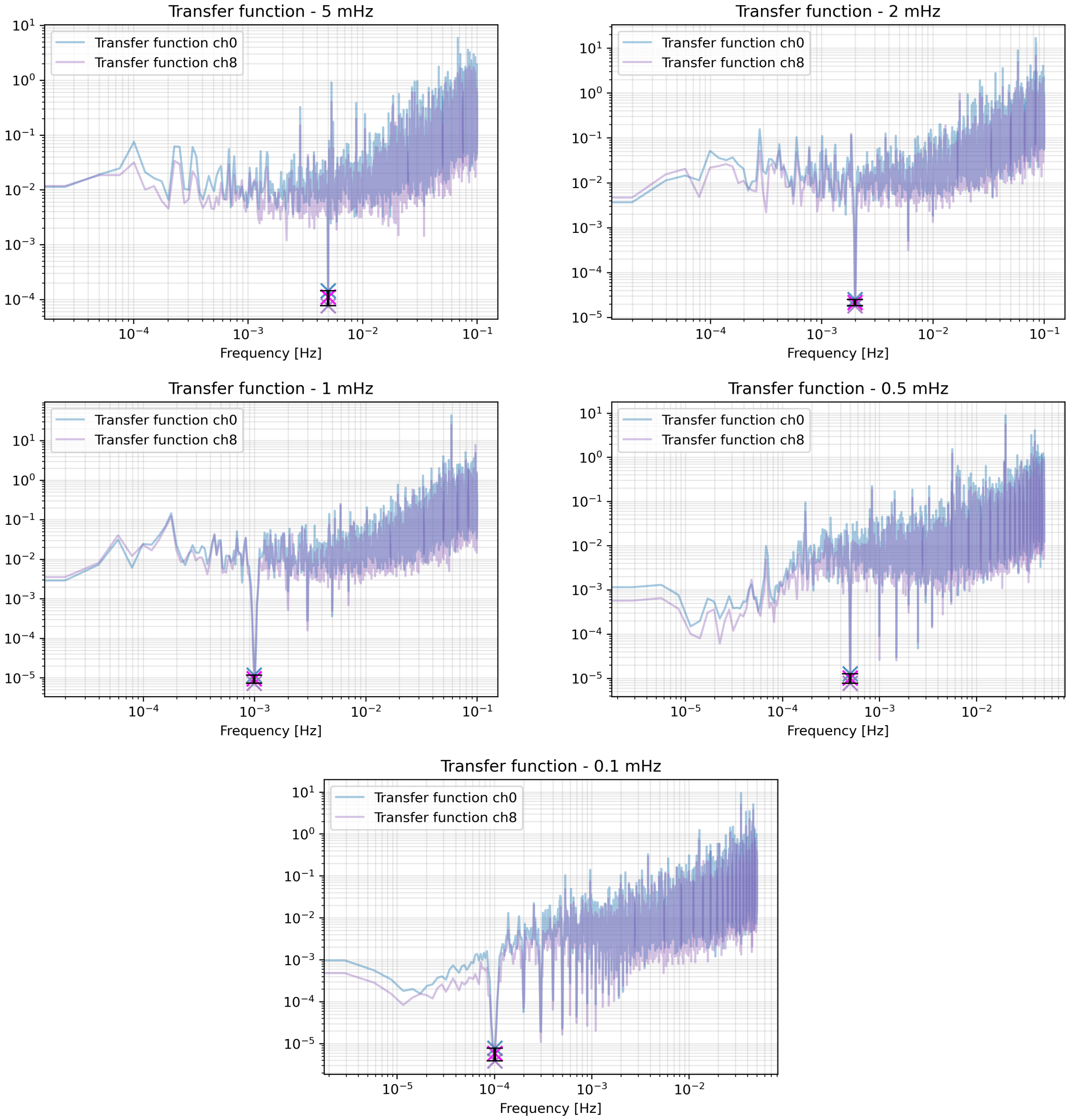

Figure 3.27: Transfer function for the aforementioned cases of study.

Table 3.2 shows the TF mean values for all the cases with a balanced WB configuration.

Frequency [mHz]	**Temperature Coefficient**
5	$(1.1 \pm 0.3)\ 10^{-4}$
2	$(2.2 \pm 0.3)\ 10^{-5}$
1	$(9.5 \pm 2.2)\ 10^{-6}$
0.5	$(10.0 \pm 2.4)\ 10^{-6}$
0.1	$(5.8 \pm 1.9)\ 10^{-6}$

Table 3.2: Mean values of the transfer functions for each case.

Figure 3.28 describes the TF results obtained for the several injections within the unbalanced WB configuration.

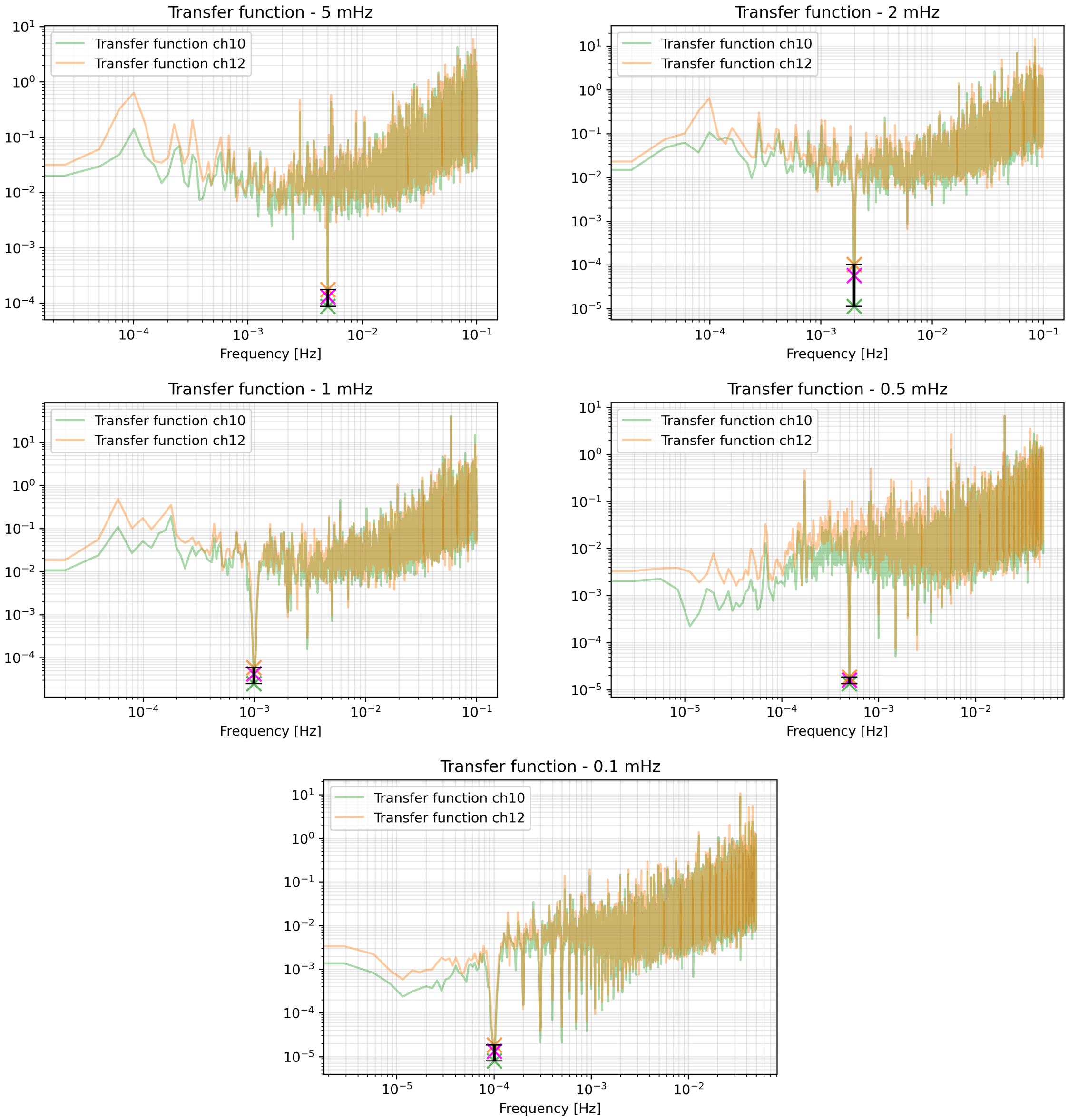

Figure 3.28: Transfer function for the aforementioned cases of study.

Table 3.3 shows the TF mean values for all the cases with an unbalanced WB configuration.

Frequency [mHz]	**Temperature Coefficient**
5	$(1.3 \pm 0.4)\ 10^{-4}$
2	$(5.7 \pm 4.5)\ 10^{-5}$
1	$(4.2 \pm 1.7)\ 10^{-5}$
0.5	$(1.6 \pm 0.3)\ 10^{-5}$
0.1	$(1.3 \pm 0.5)\ 10^{-5}$

Table 3.3: Mean values of the transfer functions for each case.

For a better comprehension and analysis of the TF results, the following figures where all the TF for both configurations are displayed is provided.

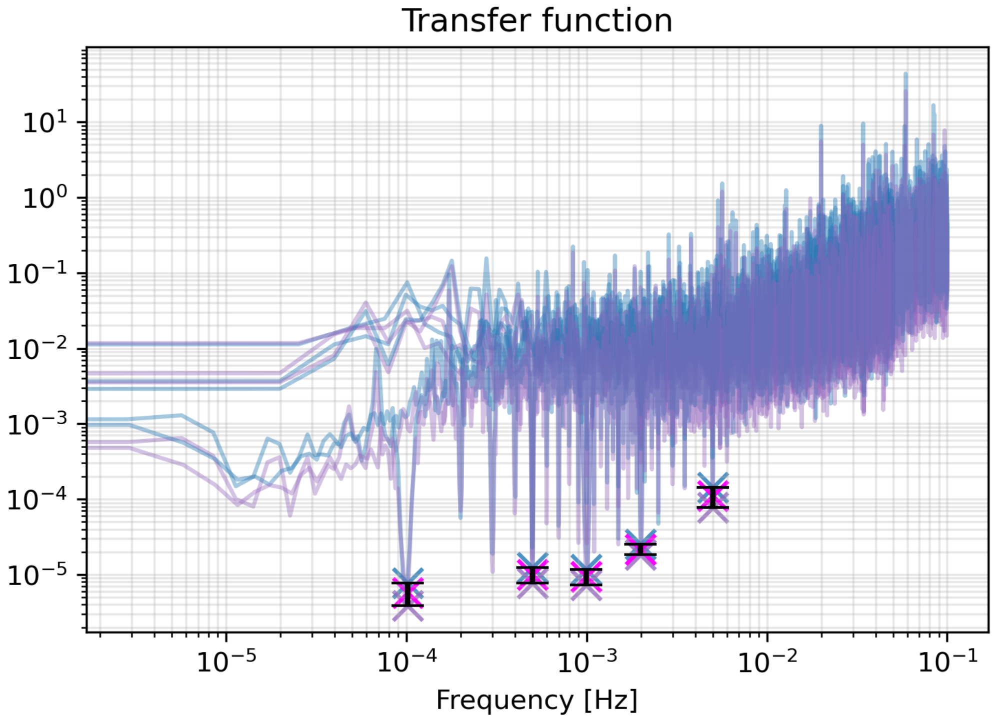

Figure 3.29: Transfer function plot for all injections for balanced WB configuration

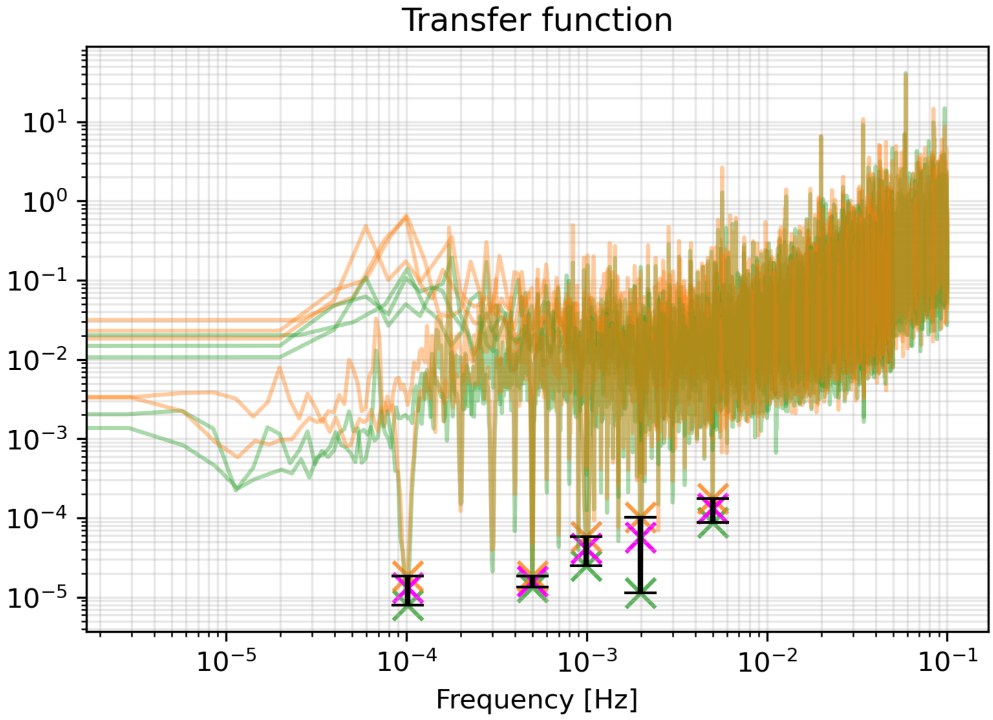

Figure 3.30: Transfer function plot for all injections with unbalanced WB configuration

For both plots, one can perceive that there is a decreasing trend of the TF value as going down on the frequency regime. The error bar present in both former figures, graphically represents the variability of TF values to indicate the error for each injection.

If the arithmetic mean is performed for both cases, we obtain a temperature coefficient of $31 \pm 19\ ppm/^{\circ}C$ for the balanced WB configuration and $52 \pm 21\ ppm/^{\circ}C$ for the unbalanced WB.

Particular attention should be given to the error bar values, as one can observe that for the balanced WB configuration the margin error seems to be barely constant. The experimental results for this case, are within a feasible margin error of the expected constant value of $23\ ppm/^{\circ}C$. The theoretical value of $23\ ppm/^{\circ}C$ is within the experimental margin error. For the unbalanced configuration, the error is variable and far from the expected constant value. It is to be noted that the theoretical value is not within the margin error previously mentioned. With this in mind, one can not define a proper value for the temperature coefficient neither conclude that this configuration provides an accurate value.

The balanced WB configuration provides a value closer to the theoretical one than the other configuration. These experimental results suggest that a proper estimation of the temperature coefficient could be performed with a balanced WB, whereas with the unbalanced configuration it is not recommended due to the changing error at each frequency. Therefore, one conclude that there are no inconsistencies in the temperature coefficient estimation procedure with the balanced WB configuration.

3.1.6. Conclusions

The purpose of this experiment was to measure the temperature coefficient of a LISA electronics prototype. This approach is useful when the noise projection analysis is performed. Such data could be beneficial in terms of providing a notion of the design and specifications of the electronics for the LISA mission.

In order to achieve this goal, a sequence of high powered square signals has been injected to the system in order to obtain the TF. When a relevant amount of power is injected in the input of the system it is easier to perceive the suppression factor that presents the output of the system. To have enough data to get a proper estimation of the temperature coefficient, several injections at different frequencies have been carried out. For all the injections, different values of power so as not to overheat the EBB and induce the degradation of the electronic devices are considered. Furthermore, two cases of study have been considered, one with a balanced WB configuration and another with an unbalanced WB.

With the obtained results, one can conclude that the proposed experiment succeed as with the balanced WB configuration the temperature coefficient meets the expected theoretical analysis. For the theoretical part, the value of the TF should be $23\ ppm/^{\circ}C$. The mean value of TF for the balanced WB configuration data is $31 \pm 19\ ppm/^{\circ}C$. For the unbalanced case, the coefficient is $52 \pm 21\ ppm/^{\circ}C$ which is far from the theoretical one. Having studied both cases, one can perceive that in order to obtain an accurate estimation of the temperature coefficient it is recommended to use a balanced WB. The unbalanced WB configuration, does not provide an accurate estimation of the temperature coefficient due to the error values which are far from a feasible margin error.

Finally, yet importantly, a different set-up could be suggested to improve the accuracy of the estimation of the TF since the system is not designed with special precision and detail to provide a high level of temperature isolation. With that in mind, I would advocate for locating the system in a non-disturb environment. The measures gathered in this dissertation are taken in the general electronics laboratory at the IEEC facilities where people are constantly going in and out the room and the air conditioning switches on and off. These considerations lead to a disturbed environment which may have influenced the measuring system.

3.2. Noise Projection

Once the temperature coefficient is defined, it is engaging to perform the noise projection analysis. This calculation can predict the noise level contribution for several noise sources. A prediction of noise levels can help tremendously with the detailed designs and mechanisms for controlling noise impacts or measuring noise reduction techniques.

An estimation of the expected temperature fluctuations in the EBB can be done by projecting the temperature fluctuations induced by the electronics using a TF. The results obtained in the following section are subjected to the air flow temperature control at IEEC facilities which are also explain in further detail in subsection 3.2.2..

3.2.1. Experiment concept

First and foremost, an interesting proposition in this thesis is to analyse the read-out noise for the LETS electronics. To achieve that goal, an experimental set-up that consists of a prototype of data acquisition that integrates inside a temperature control system is suggested. This control system is expected to stabilize the temperature through a laminar flow of air. A characterization of this system is provided in annex B. Furthermore, the study of the thermal noise contributions of the LETS EBB is conceived.

For the experimental procedure the schematics shown in Figure 3.31 are proposed. Two types of data can be distinguished. The data collected from the TB which is represented in green and the data gathered from the EBB located inside the ATCU where there is a higher controlled stable environment than in the previous set-up with the aluminium container (in orange). The data gathered with this environment is used to evaluate the read-out noise level for the LETS EBB, whereas the purpose of gathering the data from the TB focuses on proceeding with the noise projection analysis.

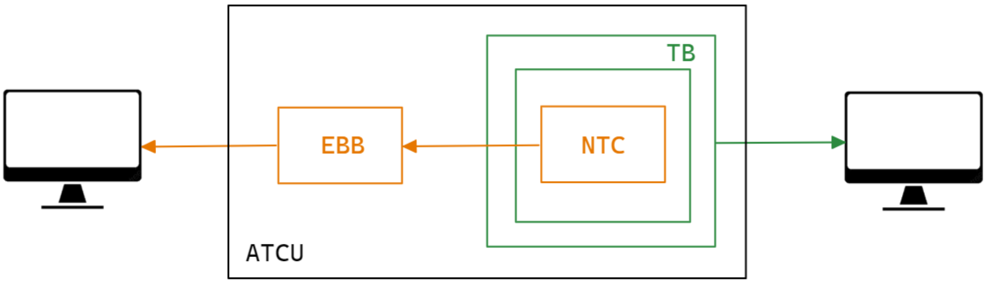

Figure 3.31: Schematics for a high controlled steady environment.

As aforementioned, a design that meets the temperature the LETS requirement is considered to evaluate the thermal noise level contribution of a LETS electronics prototype by implementing the noise projection analysis. Such a design is further detailed in [9]. It combines an active temperature control system and a passive attenuation provided by thermal shields.

Figure 3.32 represents the setup used to gather the data needed for the analysis and it is described in subsection 3.2.2..

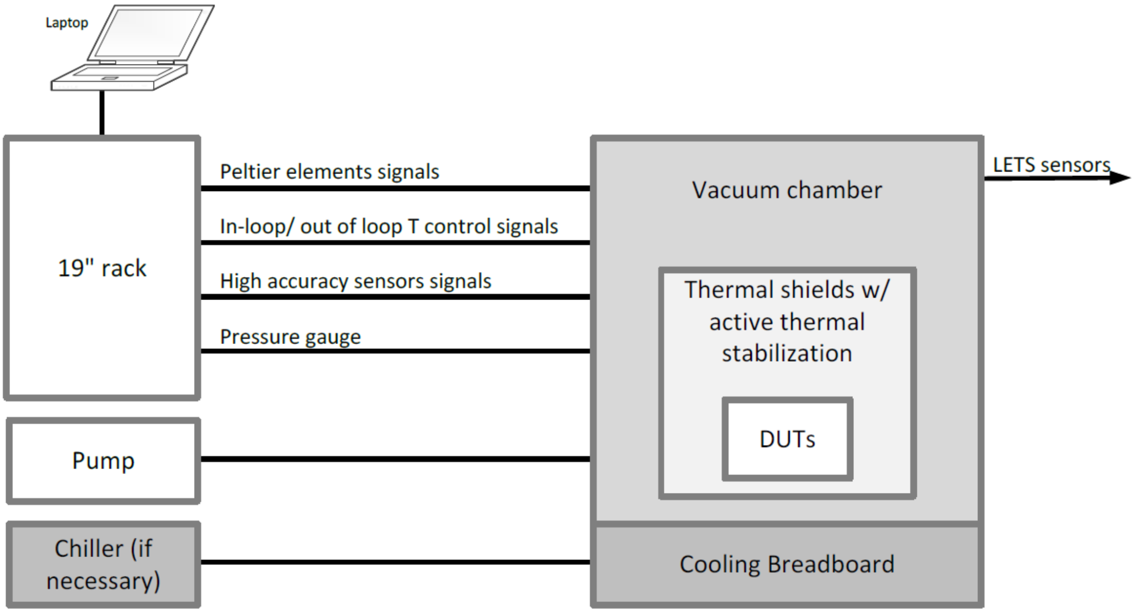

Figure 3.32: Test bench setup overview [9].

The following section provides a brief introduction of the set-up used for gathering the temperature fluctuations outside the vacuum chamber for a high controlled stable environment.

3.2.2. Set-up description

The TB consists of a vacuum chamber that houses a three-layer thermal shield assembly. The vacuum chamber is put under vacuum using a turbo pump connected to the vacuum chamber through a valve. To keep the vacuum in the chamber, the valve can be closed while the pump is switched off. The outer layer includes an active temperature control system based on Peltier elements and heat pipes as can be seen in Figure 3.33.

With that in mind, this design allows the temperature data acquisition for high controlled stable conditions aiming to simulate LISA environment conditions.

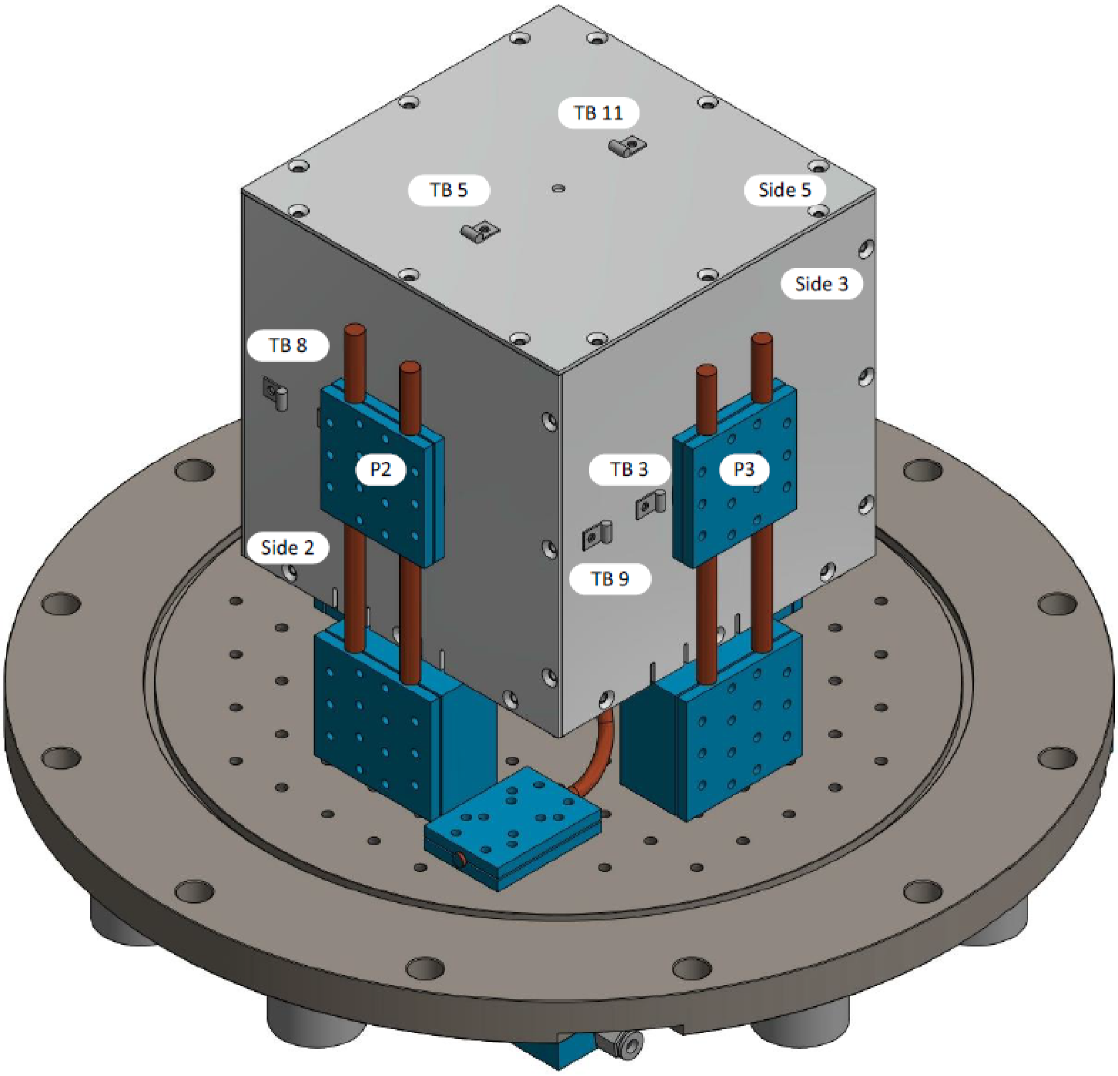

Figure 3.33: Thermal shields with Peltier elements and heat pipes [9].

As shown in Figure 3.33 the Peltier elements are designated as $Peltier(P)$ whereas the temperature sensors attached to the plate as TB.

Figure 3.34 exposes the sensors disposition. Particular relevance should be given to the sensor number 15 as it is located outside the vacuum chamber, hence it provides information about the temperature fluctuations outside the vacuum chamber where the EBB is located. The data subjected to this sensor will be used for the noise projection analysis.

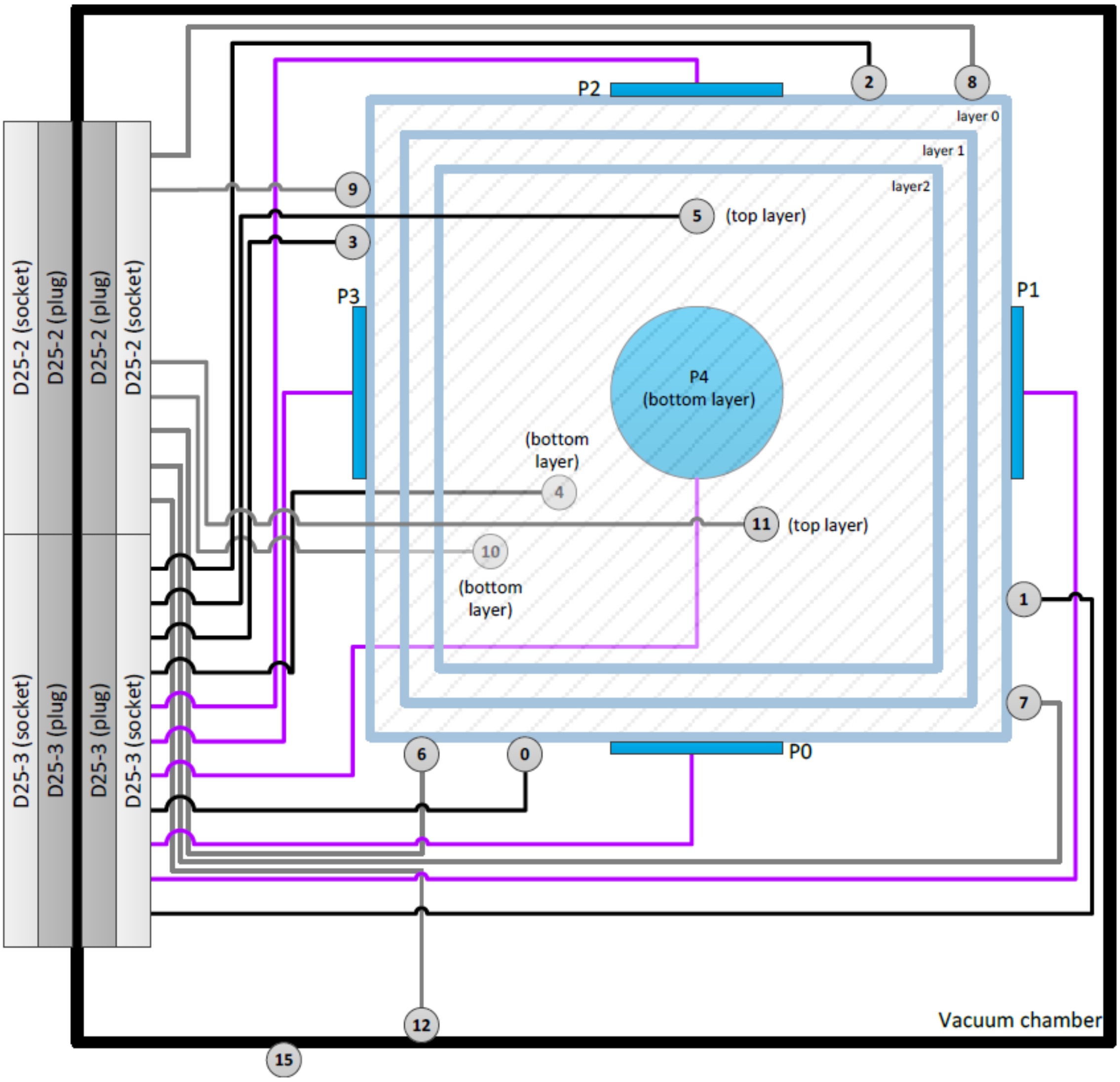

Figure 3.34: Test bench sensors disposition [9].

Further to this, there are ten temperature sensors located in the outermost shield which are represented in gray. These sensors are used to gather the temperature fluctuations inside the vacuum chamber with ultra-stable conditions.

As previously mention, we are interested in projecting the noise level contributions introduced by the external thermal fluctuations which are measured by sensor number 15. Hence, we will not be interested in the thermal data provided by the rest of the sensors.

3.2.3. Experimental Results

For this dissertation, the noise projection carried out evaluates the performance of the TMS with the TB according to the following Figure 3.35:

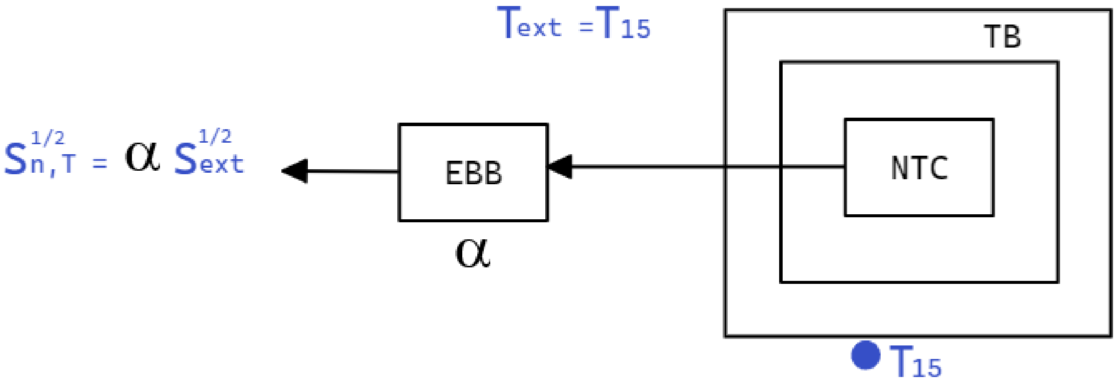

Figure 3.35: Scheme considered for the noise projection analysis.

As outlined in Figure 3.35, T_{15} depicts the temperature of the NTC sensor number 15 attached to the outer shield previously introduced in Figure 3.33. To evaluate the thermal noise contributions introduced by the EBB it is important to contemplate the temperature coefficient of the EBB for the balanced WB configuration as aforementioned. Such a parameter is defined as α and its value is $31\ ppm/°C$ as previously shown in subsection 3.1.5.3.. The unbalanced WB configuration is not considered for the noise projection analysis as it does not provide an accurate temperature coefficient estimation.

With that in mind, to compute the noise projection we proceed as follows:

$$S_{n,T}^{1/2} = \alpha\, S_{ext}^{1/2} \tag{3.11}$$

where α is the temperature coefficient of the LETS EBB prototype, $S_{ext}^{1/2}$ refers to the ASD of the temperature fluctuations outside the vacuum chamber and $S_{n,T}^{1/2}$ is the noise projection of the thermal noise contributions introduced by the LETS EBB.

A summary of the final results is shown in Figure 3.36 where the read-out noise performance of the LETS EBB and the noise projection analysis of the thermal noise contributions is presented.

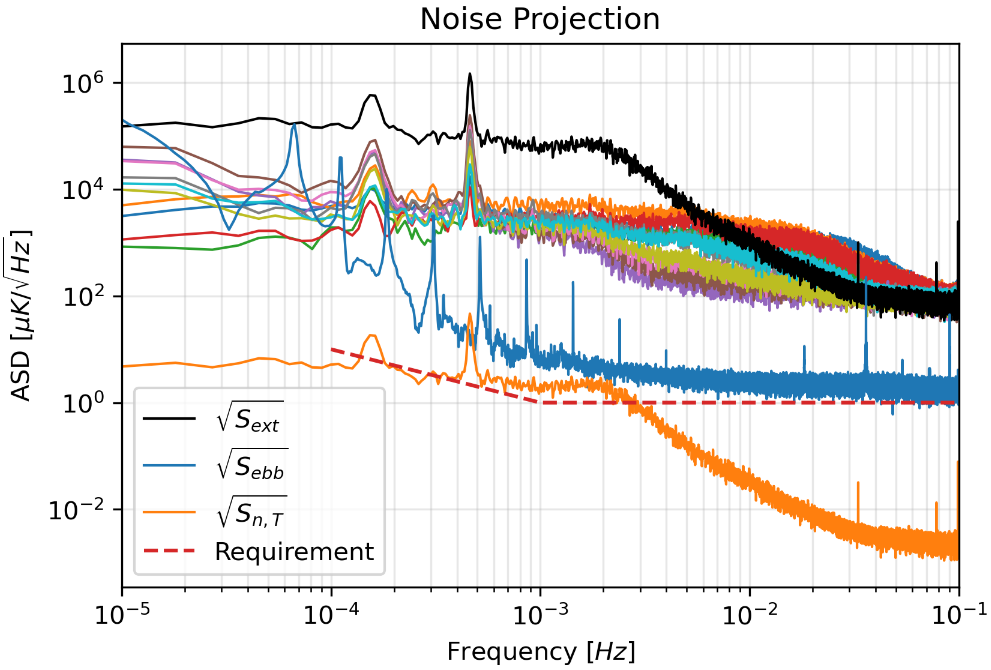

Figure 3.36: Performance of the temperature measurement system when using a sensor inside the LETS TB and a 25 k high-stability resistor connected to the LETS TMS emulating a sensor.

As outlined in the previous Figure 3.36, the order of magnitude of the read-out noise represented in blue as $\sqrt{S_{ebb}}$, is slightly above the $1\ \mu K/\sqrt{Hz}$ requirement depicted in red. Particular attention should be given to the repetitive peaks since they represent the harmonics of a sinus injection at $0.45\ mHz$. We were injecting calibration signals with the Peltiers. It is to be noted that the data analyzed is from a calibration test, hence one cannot deduce if the requirements are met.

Further to this, the $\sqrt{S_{ext}}$ presented in black is the ASD of the external thermal fluctuations outside the vacuum chamber subjected to high controlled stable conditions. As shown in the previous figure, the noise floor level at the mili-hertz frequency region is around $0.1\ K/\sqrt{Hz}$. This result suggests a high noisy environment. Moreover, two relevant peaks can be distinguished at $0.15\ mHz$ and $0.45\ mHz$ respectively. Furthermore, these peaks are also present in the ten remaining sensors of the TB. These channels which are inside the vacuum chamber still present an excess noise level.

As it stands in orange colour, the noise projection $\sqrt{S_{n,T}}$ after contemplating the temperature coefficient $31\ ppm/°C$ of the EBB previously computed experimentally, does not meet the requirement as the noise floor for the frequency band of interest is lightly above $1\ \mu K/\sqrt{Hz}$. It is to be noted that the noise projection level is below the read-out noise. The aforementioned peaks are also present in the noise projection.

3.2.4. Conclusions

This experiment was proposed to predict the noise level contribution from temperature fluctuations caused by the electronics for the LISA temperature subsystem. To achieve this goal the noise projection analysis is conceived. It is important to predict the noise levels contributions since having knowledge of these concerns could lead to an improvement of the design and specifications of the electronics for the LISA mission.

To proceed with the data analysis, a first input data measured in a stable environment is needed. To project the noise level contribution it is important to contemplate the temperature coefficient previously estimated for the LISA EBB prototype.

From the results obtained in this section, the estimated noise level contributions are slightly above the requirements of $1\ \mu K/\sqrt{Hz}$. Hence, one can state that the objective of this thesis has been almost successfully achieved.

Having considered all the aforementioned, one can conclude that if the environment conditions were improved, the LETS requirements for the LISA TMS will be met.

CONCLUSIONS

The current thesis aimed to identify the noise level contributions of the temperature fluctuations for the electronics design of the LISA mission TMS which the subsequent conclusions focuses on the theoretical and experimental results obtained in the previous chapters.

Firstly, a theoretical noise analysis of a LETS electronics prototype is carried out. The main noise contribution comes from the sensor arm and the gain drift of the ADC also dominates over the rest of components. These factors are used to simplify the theoretical temperature coefficient estimation which is of $23\ ppm/^{\circ}C$.

For the estimation of temperature coefficient, a first theoretical analysis is conceived followed by an experimental verification of the results. To gather all the processed data a design for electronic testing is proposed. As aforementioned, the experimental estimated value for the temperature coefficient with the balanced WB configuration which is $31 \pm 19\ ppm/^{\circ}C$ meets the theoretical one as the theoretical is within that margin error. It is suggested that the unbalanced WB configuration does not provide an accurate value of the temperature coefficient. All the subsequent analysis are subjected to a balanced WB configuration.

For the noise projection analysis, the set-up used is the TB provided by the IEEC facilities. To simulate the highest controlled stable conditions of the temperature fluctuations, a sensor located outside the vacuum chamber is considered. Further to this, to perform the noise projection it is to be noted that there is temperature coefficient of the EBB to be considered. This parameter relates the outside temperature fluctuations with the ones measured from the electronics itself. The resulted projection almost meets the LISA temperature subsystem requirement as the estimated noise level contribution is slightly above $1\ \mu K/\sqrt{Hz}$. Hence, one can conclude that for the LISA frequency regime, the LISA TMS does not fulfill the requirements and there is still room for improvement to achieve the proposed objective. All the data processing was done by using python.

Having considered the aforementioned results, one can predict that the next step for this dissertation would be focused on reducing the thermal noise contributions for the LISA TMS until achieving the desired goal. One may suggest that as the main noise sources are the sensor arm noise and the ADC, it would be reasonable to first start with doing some research to study if there are less noisy alternatives components to consider for the TMS.

Moreover, in space missions, the system is usually in charge of monitoring the environment, hence a precise diagnostic subsystems are required. Therefore, this approach in the TMS of LISA mission provides a notion to the study of noise contributions for the instrument noise budget which eventually will have impact on the design.

The LISA mission is an international project where exists the cooperation of several countries. The IEEC regularly takes part in a variety of ESA's projects, collaborating with the Institute of Space Science (ICE-CSIC), and evidence of such a high-quality research from both has been provided with an incredibly number of qualified scientists. Despite my involvement in such a vast area is a minor contribution, it has been a unique honour and a remarkably rewarding experience to take part of it. My enthusiasm for space science has grown and it will encourage my future studies and progress.

BIBLIOGRAPHY

[1] NASA Goddard Space Flight Center. The gravitational wave spectrum sources and detectors, January 2012. xi, 7

[2] Josep Sanjuan Munyoz. *Development and validation of the thermal diagnostics instrumentation in LISA Pathfinder*. PhD thesis, Universitat Politecnica de Catalunya (UPC), 2009. xi, 8

[3] D Reitze. 7th international lisa symposium. In *Ground based GW detectors (presentation).*, Barcelona, 2008. xi, 9

[4] et. al. ..... D.V. Martynov. Sensitivity of the advanced LIGO detectors at the beginning of gravitational wave astronomy. *Physical Review D*, 93(11), jun 2016. xi, 9

[5] C. J. Moore, R. H. Cole, and C. P.L. Berry. Gravitational-wave sensitivity curves. *Classical and Quantum Gravity*, 32, 1 2015. xi, 11

[6] et. al. ..... Amaro-Seoane. Laser interferometer space antenna, 2017. xi, 11

[7] Paul Mcnamara. Overview of lisa pathfinder. In *LISA Pathfinder*, Barcelona, 2008. xi, 13

[8] EETech Media. Ntc thermistor, 2020. Last accessed 02 July 2022. xi, 20

[9] IEEC. Lets-dlr-inst-rp-001. Aerospace mission, ESA, CA 91125, December 2019. xii, xiii, 64, 65, 66, 75

[10] Air Rover. Operation and maintenance manual sl18ba-p. Technical report, Portable Air Conditioners, 2016. xiii, 77

[11] NASA. Technology readiness level, 2022. Last accessed 09 September 2022. 5

[12] Albert Einstein. *Relativity: The Special and General Theory*. Friedr. Vieweg and Son,Braunschweig, 1920. 5

[13] Kim S. Thorne. Frequency bands, sources, and detection methods. Theoretical astrophysics, California Institute of Technology, CA 91125, July 1995. 6

[14] Fulvio Ricci and Alain Brillet. A review of gravitational wave detectors, 1997. Last accessed 09 September 2022. 8

[15] Shaode Huang, Jin Pan, and Yuyue Luo. Study on the relationships between eigenmodes, natural modes, and characteristic modes of perfectly electric conducting bodies. *International Journal of Antennas and Propagation*, 2018, 2018. 8

[16] Ferran Gibert Guitierrez. *Thermal Diagnostics Experiments for LISA Pathfinder*. PhD thesis, Universitat Politecnica de Catalunya (UPC), 2015. 10

[17] IBM Redbooks. Understanding optical communications:optical sources, 2022. Last accessed 09 September 2022. 10

[18] M. Françon, N. Krauzman, J.P. Mathieu, and M. May. *Michelson Interferometer*. CRC Press, 2021. 11

[19] Wenle Weng, James D. Anstie, Thomas M. Stace, Geoff Campbell, Fred N. Baynes, and Andre N. Luiten. Nano-kelvin thermometry and temperature control: Beyond the thermal noise limit. *Phys. Rev. Lett.*, 112:160801, Apr 2014. 18

[20] Masaya Toda, Naoki Inomata, Takahito Ono, and Ioana Voiculescu. Cantilever beam temperature sensors for biological applications. *IEEJ Transactions on Electrical and Electronic Engineering*, 12(2):153–160, 2017. 18

[21] Julius S. Bendat and Allan G. Piersol. *Engineering Applications of Correlation and Spectral Analysis*. Wiley, 2013. 44

[22] Julius S. Bendat and Allan G. Piersol. *Random data : analysis and measurement procedures*. John Wiley and SONS, 2010. 44

APPENDICES

APPENDIX A. ANALOG CHAIN BOARD SCHEMATIC

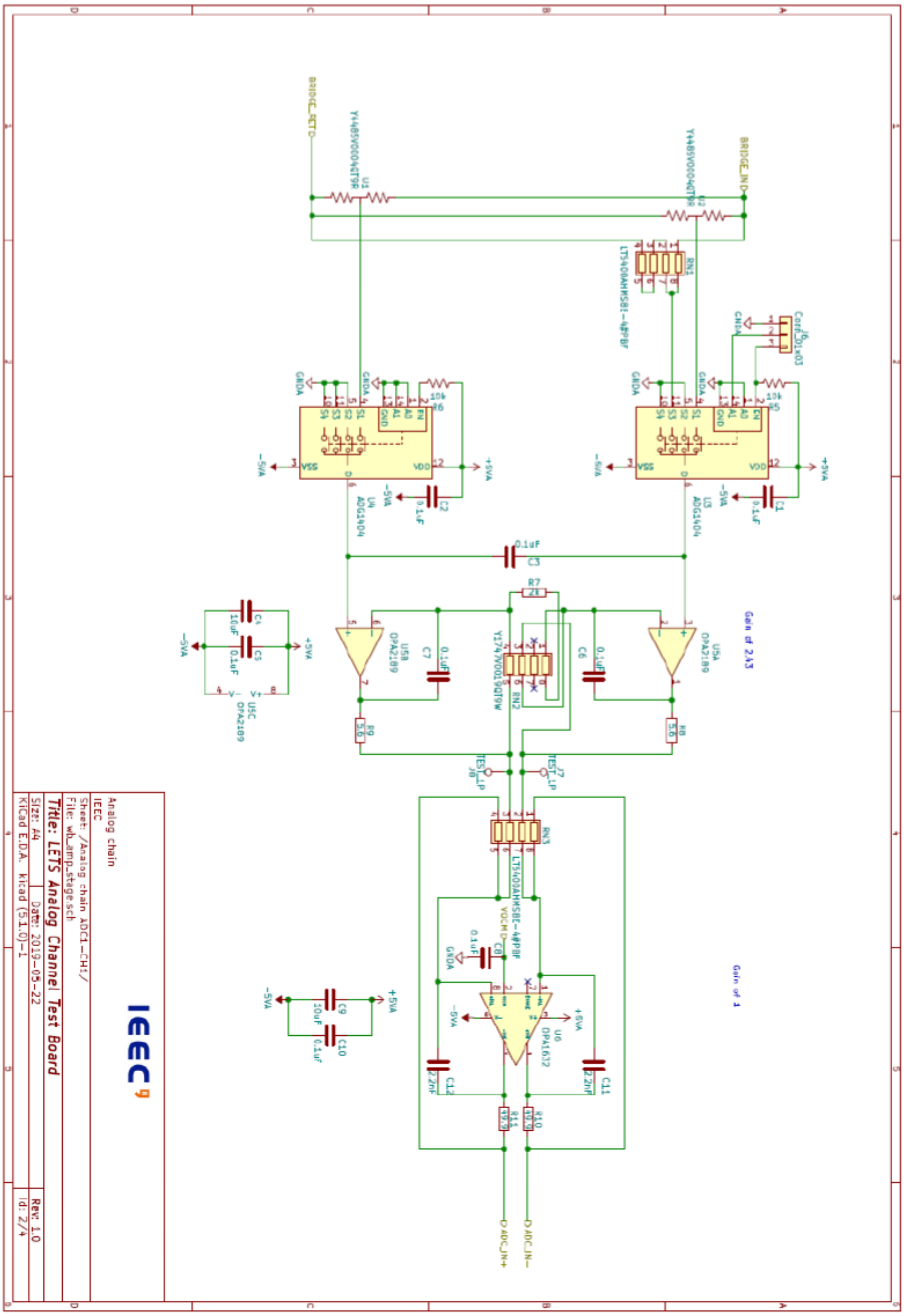

Figure A.1: Analog chain board schematic used [9]

APPENDIX B. AIR THERMAL CONTROL UNIT

B.1. ATCU characterization

The Praecis environment consists of an Air Temperature Control Unit (ATCU), an enclosure, and a single flexible duct that connects the two systems as can be seen in Figure B.1

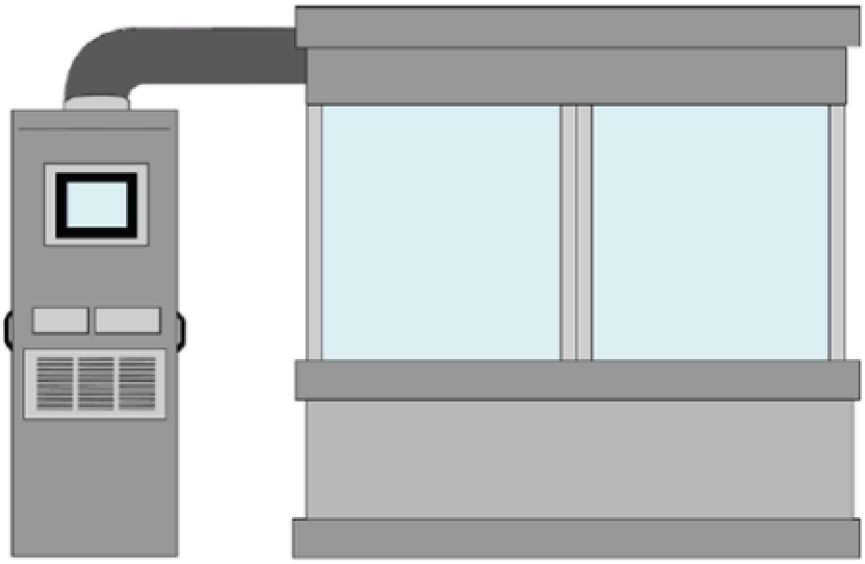

Figure B.1: ATCU schematic [10].

The Praecis ATCU is a portable air temperature control unit that provides temperature stability at any critical point in a Praecis enclosure to within $\pm\ 0.01\ °C$. The enclosure portion of the system confines the air volumes up to $25\ m^3$ sent by the ATCU.

The air from the duct to the enclosure is pushed by the fans and consequently, exhaust air from the ATCU vents via a flexible duct outside the room. The air enters the plenum of the enclosure and exits as laminar flows through perforations in the floor of the plenum. The system does not recirculate the air. If there is no plenum in the enclosure, in most instances the airflow will be turbulent. The air shower holds the desired temperature at the desired critical point in the enclosure. A temperature sensor at the critical point sends information back to a multi-loop controller, which adjusts the temperature of the ATCU air output to maintain the temperature within the enclosure.

In order to get a proper understanding of the ATCU system loop, some data have been taken into consideration.

In Table B.1 there is a summary of a few parameters that can be captured from the ATCU based on each type of data file.

H01			
CP	MC	ROOM	COLD
5	6	7	8
CPRAW	MCRAW	ROOMRAW	COLDRAW
5RAW	6RAW	7RAW	8RAW

Table B.1: Parameters obtained from H01 ATCU file

It is observable that in the H01 file there are two types of variables, the ones that are filtered versus the initial ones that have the suffix RAW.

There are eight traces used to monitor the temperature for each thermistor in use. The CPRAW (critical point) is the temperature that is expected to be controlled with the ATCU system. The MCRWA is the mixing chamber temperature which is the combination of hot and cold air streams. The ROOMRAW parameter is necessary when long-term changes in the environment are predicted. The COLDRAW is the cold air generated by a Carnot-cycle heat pump and the FAN is dedicated to monitoring the fan voltage.

For the data file type $H02$ the parameters obtained are as follows:

H02		
Outside Loop Input	Outside Loop Setpoint	Outside Loop Output
Outside Loop P	Outside Loop I	Outside Loop D
Inside Loop Input	Inside Loop Setpoint	Inside Loop Output
Inside Loop P	Inside Loop I	Inside Loop D

Table B.2: Parameters obtained from H02 ATCU file.

Regarding the data obtained from the ATCU system, it is possible to estimate the relation between some of the variables and make a first model loop characterization of the ATCU system.

Several assumptions can be extracted from the ATCU data:

- Outside Loop Input = CPRAW

- Outside Loop Output = [-4,4]

- Inside Loop Output = FAN = [1,5];

- Inside Loop Input = MCRAW

- Inside Loop Setpoint = Outside Loop Setpoint + Outside Loop Output

Figure B.2 represents the first loop characterization for the ATCU system loop. Whereas C1 is the outside controller, C2 is the inside controller, A is the fan actuator and P is the plant of the system.

In the temperature control system, the primary value to set is the Outside Loop Setpoint which indicates the objective temperature. When the setpoint value is compared to the controlled temperature CPRAW, the remaining error is minimized by the C1 and its output is used to compute the Inside Loop Setpoint which is the sum of the Outside Loop Setpoint and the Outside Loop Output. Afterward, this inner setpoint is also compared with the mixing chamber temperature and its error is minimized too and the FAN proceeds according to this value. The FAN voltage which is the Inside Loop Output parameter is limited by two saturations points, $1\ V$ and $5.5\ V$. Once the controlled system is defined, the plant of the system which has not been characterized due to its complex structure proceeds as follows to close the ATCU system loop.

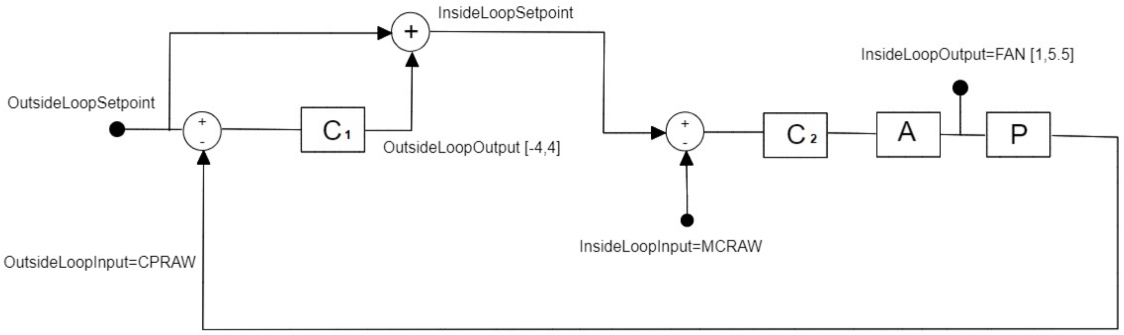

Figure B.2: First model characterization of the ATCU system loop.